



0D/3D CNQDs/CuFe₂O₄/Cu⁰ heterostructures as broad spectrum photocatalyst for efficient 5-fluorouracil degradation: Structural evolution and relay oxidation process

Anqi Wang^a, Shuya Guo^{a,b}, Manman Xu^a, Cuilin Meng^a, Haida Zhu^a, Tong Zheng^c, Hui Wang^e, Kai Wang^a, Wei Shi^f, Xingxin Liu^a, Xiaolong Song^a, Zhaofeng Chang^{c,d,*}

^a Research Center for Eco-environmental Engineering, Dongguan University of Technology, Dongguan 523808, China

^b College of Chemistry and Environmental Engineering, Shenzhen University, Shenzhen 518060, China

^c State Environmental Protection Key Laboratory of Environmental Pollution Health Risk Assessment, South China Institute of Environmental Sciences, Ministry of Ecology and Environment, Guangzhou 510655, China

^d Faculty of Environmental Science & Engineering, Kunming University of Science & Technology, Kunming 650500, China

^e Institute of Chemistry, Humboldt University of Berlin, Berlin 12489, Germany

^f Guangzhou Water Science Research Institute, Guangzhou 510220, China

ARTICLE INFO

Keywords:

CNQDs/CuFe₂O₄/Cu⁰

Broad spectrum photoresponse

PMS induced strategy

Dual Z-scheme heterostructures

DFT computation

ABSTRACT

Undesirable solar energy absorption, poor charge transfer efficiency, and sluggish metallic ions redox cycle are three pressing problems, restricting the application of photocatalysis and peroxymonosulfate (PMS) techniques. Herein, an interface engineering of g-C₃N₄ quantum dots anchoring on the CuFe₂O₄/Cu⁰ hollow microspheres (CNQDs@CFO) was developed to construct a novel 0D/3D broad-spectrum-response photocatalyst. In the relaying PMS-photocatalysis process, 30 μM 5-fluorouracil (5-FLU, 50 mL) was degraded by 99.4 % in 60 min with 0.2 g L⁻¹ 1.0CNQDs@C₁F₁O and 0.3 mM PMS. The reusability test showed that 1.0CNQDs@C₁F₁O maintained superior performance with a 5-FLU removal of 92.6 % after the fifth run. Meanwhile, this newly-designed material can be applied in a large temperature and pH range, and even actual water bodies with strong environmental adaptability. Theoretic and experimental analysis demonstrated that the CNQDs and Cu⁰ sites on CNQDs@CFO promoted the earlier PMS activation, and then dual Z-scheme heterostructures (CNQDs/CuFe₂O₄/CuO) was established, boosting the follow-up photocatalytic activity.

1. Introduction

As a revolutionary breakthrough in medical field, anticancer drugs (ADs) have saved millions of lives by virtue of their powerful function mechanism to curb the malignant growth of cancer cells [1,2]. In recent years, with the increasing incidence of cancer, the demand and consumption for these pharmaceutical products is surging rapidly around the world [3]. 5-Fluorouracil (5-FUL) is one of the most representative cytotoxic drugs used in anticancer therapies [4,5]. The non-selective attack of 5-FUL on cancer cells and healthy cells makes it present mutagenetic and teratogenic properties [6–8]. As assessed by the International Agency for Research on Cancer (IARC), the toxicity threshold of 5-FUL is 230 ng L⁻¹ [9]. Because it is hard to be completely metabolized, 5-FUL will be excreted with human waste after

administration, and subsequently discharge into the urban or hospital sewage pipe network [10–12]. However, conventional techniques employed in wastewater treatment plants (e.g., coagulation, flocculation, filtration or bio-treatment) are inefficient for eradicating this stable compound, leading to the release of 5-FUL into nature water bodies persistently [13–15]. Nowadays, the lack of clear guidelines on permissible limits for the emerging pharmaceutical pollutants in the environment has aggravated the seriousness of their contamination. Hence, it is an urgent task to develop cost-effective technologies for purification of 5-FUL-containing wastewater to shrink its environmental footprint.

So far, many studies have shown that the combination of peroxymonosulfate (PMS) with photocatalysis to establish a coupling oxidation system seems to be the preferable choice to greatly boost up the

* Corresponding author at: State Environmental Protection Key Laboratory of Environmental Pollution Health Risk Assessment, South China Institute of Environmental Sciences, Ministry of Ecology and Environment, Guangzhou 510655, China.

E-mail address: changzhaofeng545@163.com (Z. Chang).

<https://doi.org/10.1016/j.apcatb.2022.122117>

Received 1 July 2022; Received in revised form 22 October 2022; Accepted 25 October 2022

Available online 3 November 2022

0926-3373/© 2022 Elsevier B.V. All rights reserved.

performance of oxidation degradation [16–18]. Benefiting from the synergistic effect between the two AOPs technologies, on the one hand, photoexcited electrons can be captured by PMS and high valence states ($M^{(n+1)+}$) to produce $SO_4^{\cdot-}$ and low valence states (M^{n+}), increasing the separation rate of photogenerated carriers [19,20]. On the other hand, the accelerated redox cycle of $M^{n+}/M^{(n+1)+}$ and enhanced photocatalytic activity in turn promotes the decomposition of PMS to continue [21]. Interestingly, in addition to improving the oxidation degradation efficiency, the PMS-photocatalytic process is also to be a newly developed method to modulate heterostructure through altering valence, generating new metal oxide composites. For example, Zhao et al. [22] reported a PMS induced strategy for valence heterojunction construction under visible light irradiation, which could realize rapid photoinduced charge separation, thereby raising photocatalytic activity dramatically. Thus, it is desirable to design a material for the PMS-photocatalysis coupling system to synergistically degrade stubborn pollutants, and evolve its structure during reacting with PMS to form a more favorable heterojunction for photocatalysis, so then effectively connecting PMS and photocatalytic process.

Indeed, the key point for the PMS-photocatalytic technology lies in the rational design of photocatalysts. Recently, the establishment of Z-scheme charge transfer system has been received increasing attention and recognized as a useful means to achieve maximal photocatalytic activity. This is because this type heterojunction can well promote spatial charge separation and retain the strong reduction and oxidation potential of photoinduced electrons and holes [23–25]. Moreover, the morphological control has also been turned out to be a significant tool to optimize the catalytic properties by tailoring materials into a designated structure [26,27]. Thereinto, hollow microsphere, a kind of popular structure for photocatalysis, has the features of huge internal space and nanosized shell thickness, which enables light to be reflected multiple times in the inner cavities to improve the exploitation of solar energy [28,29]. As for PMS activation, this structure has high specific surface area, abundant accessible active spots, and short distance for mass transfer [30]. In this context, to further unlock the potential of PMS-photocatalysis system, the struggle to design a hollow microspherical photocatalyst with Z-scheme heterojunction is a worthwhile step.

Transition mixed metal spinels commonly demonstrate an impressive performance in catalytic activation of PMS due to the favorable electron transfer properties promoted by self-redox cycle of bimetals [31,32]. Especially, strong magnetism, slight metal leaching rate, and low toxicity make $CuFe_2O_4$ hold enormous applied potentiality in controlling water pollution, whereas the $CuFe_2O_4$ particles are prone to aggregation, lessening seriously the available active sites [33]. Meanwhile, as a narrow bandgap semiconductor, $CuFe_2O_4$ shows a certain response to visible light, but the leading problem of easy recombination of photogenerated electrons and holes precludes it being an effective visible-light-driven photocatalyst [34,35]. It is noteworthy that g- C_3N_4 quantum dots (CNQDs) has recently aroused considerable interest in photocatalysis because of its suitable band potentials, significant quantum confinement effect, up-conversion effect, and sensitization effect [36,37]. Accordingly, CNQDs emerges as a capable decorator to modify semiconductor for elevating broad spectrum photocatalytic performance. Considering above inspiring studies, anchoring CNQDs onto the morphologically engineered $CuFe_2O_4$ to construct a novel 0D/3D nanojunction architecture, featuring prominent PMS activation and photocatalytic ability, is prospective and advisable.

In this work, we document an attempt to develop a segmented coupling system of PMS oxidation and visible-light photocatalysis, where 0D CNQDs decorated 3D $CuFe_2O_4/Cu^0$ hollow microspheres (CNQDs@CFO) were controllably synthesized as broad spectrum photocatalyst. In the beginning of the degradation reaction, CNQDs and Cu^0 active sites could promote the activation of PMS. Then benefiting from the generation of new oxidation state via PMS induced strategy, dual Z-scheme heterojunction was formed, effectively strengthening the late

photocatalytic process. The physical and chemical natures of the obtained CNQDs@CFO composites were analyzed by a series of characterization techniques. To evaluate the photocatalytic activity of the prepared materials, 5-FLU, a frequently reported cytotoxic ADs throughout the world, was chosen as the target contaminant. Afterwards, the factors influencing 5-FLU elimination in the CNQDs@CFO/PMS/vis system, such as incipient pH value, temperature, coexisting ions and organics, water substrate, were investigated to explore its environmental compatibility. Besides, in the oxidation degradation process, the produced decomposition intermediates together with major active substances were also identified. Eventually, the underlying synergistic mechanism for the enhanced removal of 5-FLU in the proposed PMS-photocatalysis system was systematically clarified based on the theoretical computation and experiment results.

2. Experimental

2.1. Chemicals and characterization

The specific specifications and sources of chemical reagents used in this study are reported in Text S1 of the [Supplementary Information](#). The synthesized materials were characterized by the combination of field-emission scanning electron microscope (FESEM), transmission electron microscopy (TEM), high-resolution transmission electron microscopy (HRTEM), energy dispersive spectrometer detector (EDS), X-ray diffraction (XRD), Fourier transform infrared spectroscopy (FTIR), N_2 adsorption-desorption, X-ray photoelectron spectroscopy (XPS), inductively coupled plasma-atomic emission spectrometry (ICP-AES), vibrating sample magnetometer (VSM), photoluminescence emission spectroscopy (PL), time-resolved transient photoluminescence spectra (TRPL), ultraviolet-visible diffuse reflectance spectra (UV-vis DRS) and electrochemical analysis, and the details can be found in Text S2.

2.2. Photocatalyst synthesis

CFO: In a typical procedure, the appropriate amount of $Fe(NO_3)_3 \cdot 9H_2O$ and $Cu(NO_3)_2 \cdot 3H_2O$ were consecutively added into the beaker containing isopropyl alcohol (52.5 mL) and glycerol (7.5 mL) and mixed under magnetic agitation until the precursors of iron and copper were dissolved totally. Subsequently, 1 mL of distilled water was slowly injected into the homogeneous solution obtained above. After ultrasonic dispersion for 10 min, the mixture was poured into a 100 mL Teflon-lined stainless steel autoclave, maintaining at 190 °C for 12 h to perform solvothermal reaction. Finally, the acquired product was naturally cooled down from high temperature, then collected after multiple washing-centrifuging cycles with distilled water and anhydrous alcohol, and dried in an oven at 60 °C overnight. The synthesized bimetallic composites with different precursor molar ratio of $[Cu^{2+}]/[Fe^{3+}] = 4:1, 1:1$ and $1:4$ were denoted as C_4F_1O , C_1F_1O and C_1F_4O , respectively. CNQDs could be obtained based on the previous literature [38], and the preparation details are provided in Text S3.

CNQDs@CFO: A specific quality of the previously prepared CNQDs and CFO were introduced into 40 mL of ethanol-water mixture with equal volume ratio, which was then ultrasonically treated for 30 min and stirred for another 12 h at normal temperature to ensure CNQDs and CFO integrated tightly. After that, raising the temperature to 70 °C, a further mixing for the suspended liquid was carried out in water bath until the solvents was thoroughly evaporated, and then the dried solid was sintered at 350 °C in a 5 % H_2/N_2 reducing atmosphere at a ramping rate of 2 °C min^{-1} and held there for 3 h to obtain the CNQDs@CFO composites. Rinse using ethanol and pure water repeatedly to make certain that the final substance was free of impurities. The fabricated CNQDs@CFO samples with various CNQDs mass ratios at 0.1 %, 0.5 %, 1.0 %, and 2.0 % were denoted as 0.1CNQDs@CFO, 0.5CNQDs@CFO, 1.0CNQDs@CFO, and 2.0CNQDs@CFO, respectively.

2.3. Degradation procedures

The catalytic properties of CNQDs@CFO composites in the coupling oxidation system were evaluated with reference to the elimination efficiency of a 5-FLU aqueous solution under the illumination of visible light. All degradation experiments were performed in an XPA-7 multi-channel photochemical apparatus equipped with condensate water recovery system to remain an even temperature (Xujiang Electromechanical Plant, Fig. S1). In each test, 10 mg of catalyst powder was added to 50 mL of pollutant solution with a 30 μ M working concentration and then dispersed by ultrasound for 30 min. After that, the formed suspension was stirred at a uniform speed in an unlighted area for 60 min to reach an adsorption-desorption equilibrium of 5-FLU molecules on the material surface. A 350 W Xe lamp with a 420 nm cutoff filter, surrounded by a quartz jacket filled with circulating cooling water, was switched on as a visible light source, and meanwhile, the photocatalytic reaction was started by injecting 0.3 mM of PMS. Intermittently, 1.5 mL of sample was withdrawn using a syringe needle, quenched with 50 μ L of methanol immediately and passed through a 0.22 μ m Millipore filter to separate any suspended particles for subsequent analysis. The time dependent reduction of 5-FLU was determined by monitoring its instantaneous concentration at different time point on a Thermo UltiMate 3000 HPLC. Besides, the mineralization rates, chief ROS, degradation pathways, catalytic stability, residual PMS concentration, and free radical concentration were also explored, and the detailed analytical methods and operating conditions are appended in Text S4–S7.

2.4. Computational methods

The theoretical calculations of PMS adsorbed-dissociated process and the electronic structure and active sites of materials were conducted based on density functional theory (DFT) calculation using the Vienna Ab initio Simulation Package (VASP) code and calculation methods are described in the Text S8.

2.5. Optical parameters

According to previous studies [39–43], the catalyst optical parameters, including absorption and scattering coefficients in the aqueous suspension, reactor optical thickness, and total rate of photon absorption were evaluated. The total absorption of the radiant energy, depending on the reactor geometry and material optical properties, was determined by using the six-flux absorption-scattering model. The experiments were carried out at different catalysts loadings (0.1–0.4 g L⁻¹). In addition, the calculations were performed hypothesizing the solar radiation in the visual spectrum (400–800 nm) on a plane tilted 37° towards the sun.

Firstly, based on the experimental data, the non-specific extinction coefficient (β_λ) at each concentration could be obtained from the following Eq. (1):

$$\beta_\lambda = 2.303 \left(-\frac{\text{ABS}_\lambda}{L} \right) \quad (1)$$

where L represents cell path length (m) and ABS_λ is absorbance reading. Then, linear regression of the calculated β_λ for different concentrations were applied to get the specific extinction coefficient (β^*_λ).

Subsequently, for calculating the non-specific absorption coefficient (κ^*_λ), the Eqs. (2)–(4) were used. Similarly, the specific absorption coefficient was calculated by performing a standard linear regression over the k_λ .

$$(S + K) = \log(1/T)/L \quad (2)$$

$$\frac{S}{S + K} = \frac{R}{1 - T} \quad (3)$$

$$k^*_\lambda = K^*/3 \quad (4)$$

For a given catalyst with particular concentration, the specific scattering coefficient (σ^*_λ) was defined as Eq. (5):

$$\sigma^*_\lambda = \beta^*_\lambda - \kappa^*_\lambda \quad (5)$$

The optical thickness (τ_{app}), a dimensionless parameter, was calculated using the average of β^*_λ , κ^* , and σ^*_λ obtained previously, as shown in Eqs. (6–8):

$$\beta^* = \int \beta^*_\lambda W_\lambda d\lambda / \int W_\lambda d\lambda \quad (6)$$

$$\kappa^* = \int \kappa^*_\lambda W_\lambda d\lambda / \int W_\lambda d\lambda \quad (7)$$

$$\sigma^* = \int \sigma^*_\lambda W_\lambda d\lambda / \int W_\lambda d\lambda \quad (8)$$

After the above data were obtained, the values of τ_{app} were calculated according to the following Eqs. (9)–(13):

$$p = \frac{\sigma^*}{6\beta^*} \quad (9)$$

$$K = \frac{\kappa^* \kappa^* + 3/2 \sigma^* p}{\kappa^* + 1/2 \sigma^* p} C_{\text{cat}} \quad (10)$$

$$S = p \sigma^* \frac{\kappa^* + 3/4 \sigma^* p}{\kappa^* + 1/2 \sigma^* p} C_{\text{cat}} \quad (11)$$

$$\omega_{\text{corr}} = \frac{S}{S + K} \quad (12)$$

$$\tau_{\text{app}} = l(S + K) \sqrt{1 - \omega_{\text{corr}}^2} \quad (13)$$

Next, the LVRPA was defined as Eqs. (14)–(16):

$$\lambda_{\omega_{\text{corr}}} = \frac{1}{(S + K) \sqrt{1 - \omega_{\text{corr}}^2}} \quad (14)$$

$$\gamma = \frac{1 - \sqrt{1 - \omega_{\text{corr}}^2}}{1 + \sqrt{1 - \omega_{\text{corr}}^2}} \quad (15)$$

$$\begin{aligned} \text{LVRPA} = [I/\lambda_{\omega_{\text{corr}}} \omega_{\text{corr}} (1 - \lambda)] & \left[\left(\omega_{\text{corr}} - 1 \right. \right. \\ & + \left. \sqrt{1 - \omega_{\text{corr}}^2} \right) e^{-x/\lambda_{\omega_{\text{corr}}}} + \gamma \left(\omega_{\text{corr}} - 1 \right. \\ & \left. \left. - \sqrt{1 - \omega_{\text{corr}}^2} \right) e^{-x/\lambda_{\omega_{\text{corr}}}} \right] \end{aligned} \quad (16)$$

Finally, the LVRPA values were further employed to calculate TRPA (Eq. (17)).

$$\text{TRPA} = \int \text{LVRPA} \cdot dx \quad (17)$$

3. Results and discussion

3.1. Morphologies and structures

The procedures for the preparation of the hierarchical CNQDs@CFO hollow microspheres photocatalysts are schematically depicted in Fig. 1a. The zeta potentials of CNQDs and CFO were −21.8 mV and 9.9 mV (Fig. S2), respectively, indicating that the CNQDs and CFO could show electrostatic attraction in mixed solution. Then, the electrostatic self-assembly product was calcined in a H₂-reducing atmosphere, and chemically bonded interfaces would be formed, which could tightly combine the CNQDs with the 3D hierarchical CFO microspheres.

The appearance, structure, and element distribution of the prepared photocatalysts were initially examined by SEM, TEM, HRTEM, and EDS-

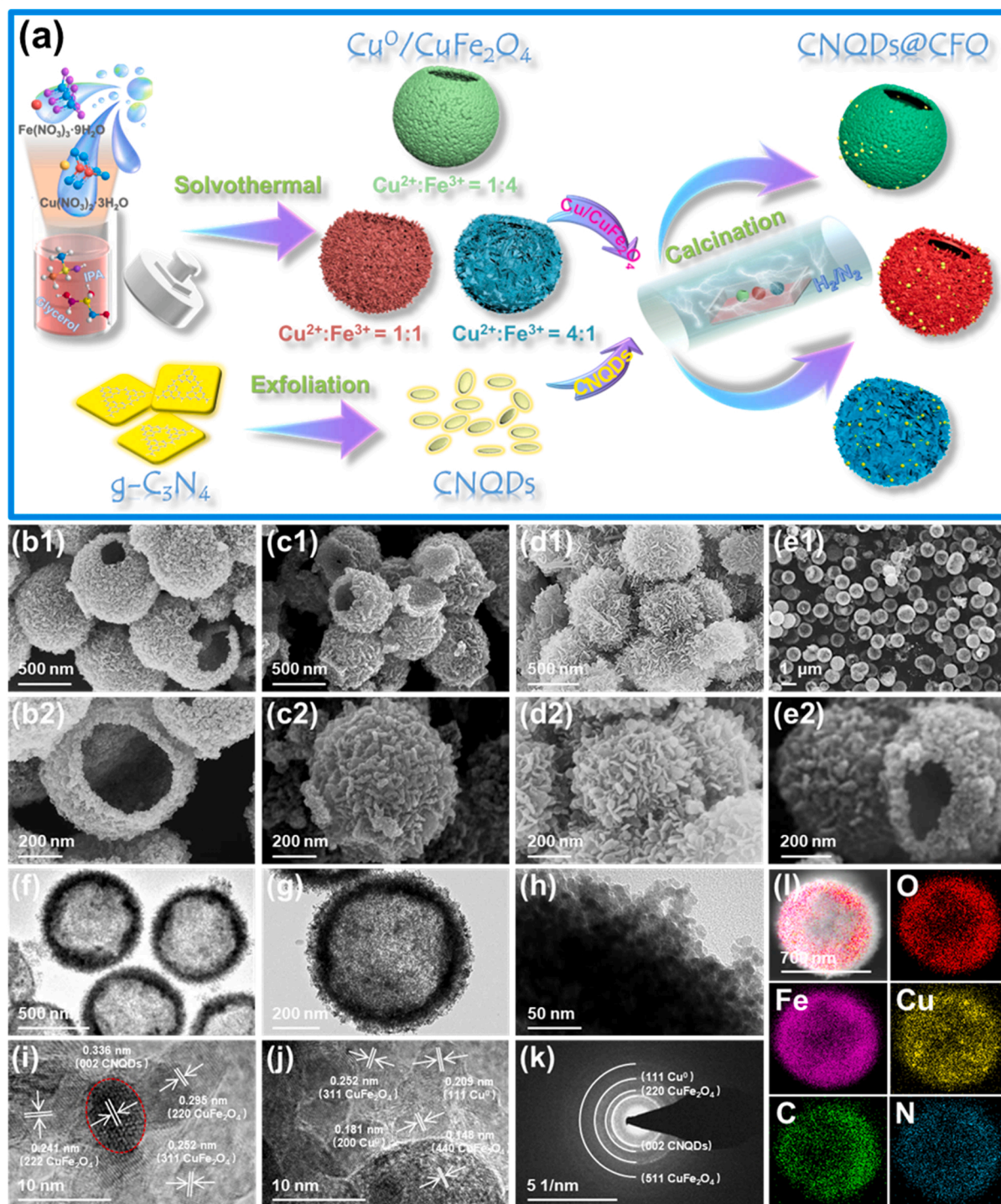


Fig. 1. (a) Schematic illustration of the synthetic route for CNQDs@CFO. SEM images of (b1 and b2) C_1F_4O , (c1 and c2) C_1F_1O , (d1 and d2) C_4F_1O , and (e1 and e2) CNQDs@ C_1F_1O . (f–h) TEM images, (i and j) HRTEM images, (k) SAED pattern, and (l) EDS elemental mapping images of the CNQDs@ C_1F_1O photocatalyst.

mapping images. As present in Fig. 1b and c, the C_1F_4O and C_1F_1O samples were observed to be regular spherical with an apparent cavity structure. In careful observation, with the increment of Cu content, the surface of the obtained material becomes coarser, where many clear ravines were shaped by granule packing. Furthermore, when the precursor ratio of Fe/Cu rose to 1:4, the outer surfaces of C_4F_1O were composed of numerous nanosheets (Fig. 1d). Interestingly, after loading CNQDs, the synthesized CNQDs@ C_1F_1O still maintained a spherical architecture with uniform size, and no significant change in the framework was found (Fig. 1e).

The TEM image shown in Fig. 1f and g verified again the hierarchical hollow feature of CNQDs@ C_1F_1O microspheres. Its mean diameter and shell thickness were near to 730 ± 20 nm and 100 ± 10 nm, respectively. The small particles that made up these microspheres could be clearly seen in the magnified image (Fig. 1h). The lattice fringes with spacing of 0.336, 0.209, 0.181, 0.295, 0.252, 0.241, and 0.148 nm were easily discernible in the HRTEM image (Fig. 1i and j), corresponding to the (002), (111), (200), (220), (311), (222), and (440) facets of CNQDs, Cu^0 , and $CuFe_2O_4$, respectively. Likewise, a polycrystalline nature of CNQDs@ C_1F_1O could be disclosed by the SAED pattern (Fig. 1k), in

which the diffraction rings were indexed to (002), (111), (220), and (511) planes of CNQDs, Cu^0 , and CuFe_2O_4 , respectively. The EDS mapping characterization (Fig. 11) demonstrated that Fe, Cu, O, C and N as the constituting elements were evenly distributed across the produced composite surface, suggesting the successful combination of CNQDs and $\text{C}_1\text{F}_1\text{O}$.

The XRD spectra of the synthesized materials were plotted to analyze their crystalline phases (Fig. 2a and b). For the CFO with different Fe/Cu ratios, some diffraction peaks were observed at 30.2° , 35.5° , 43.2° , 57.1° , 62.7° and 74.2° , matching well with (220), (311), (400), (511), (440) and (533) planes of cubic spinel CuFe_2O_4 phase (JCPDS No. 77-0010). Besides, three feature signals appeared at 43.3° , 50.4° and 74.1° with reflections (111), (200) and (220) in the light of JCPDS No. 99-0034 represented the metallic copper, which could be ascribed to the reduction of excess Cu^{2+} in H_2/N_2 atmosphere. From the XRD patterns, it can be clearly seen that by raising the proportion of Cu precursor to a higher level ($\text{C}_4\text{F}_1\text{O}$), Cu^0 gradually became the major phase in the composite. Consequently, the phase structures of the obtained CFO were all hybrids of CuFe_2O_4 and Cu^0 . For the $\text{C}_1\text{F}_1\text{O}$ modified by 0.1–2 % CNQDs, nevertheless, no additional peak for CNQDs was detected in these samples. This might be a result of the small size, limited loading amount, and fine dispersion of CNQDs. But the remarkable thing was that with the increase of CNQDs content, the characteristic peak intensities of $\text{C}_1\text{F}_1\text{O}$ obviously decreased, indirectly proving that the CNQDs was covered on the $\text{C}_1\text{F}_1\text{O}$ surface.

The FTIR spectra of the CNQDs, $\text{C}_1\text{F}_1\text{O}$, and $1.0\text{CNQDs}@ \text{C}_1\text{F}_1\text{O}$ materials were carried out to characterize their chemical bonding and functional groups. From Fig. 2c, the feature absorption band between 1200 and 1700 cm^{-1} (i.e., 1243, 1321, 1416, 1463, 1574, and 1634 cm^{-1}) could be observed for the pure CNQDs, which matched well with the C-N(C)-C or C-NH-C stretching vibration modes in C-N heterocycles [44]. Besides, the typical breathing vibration peak of triazine units, locating at 808 cm^{-1} was also found [45]. The spinel-type $\text{C}_1\text{F}_1\text{O}$ sample exhibited an intensive signal at the wavenumber of 572 cm^{-1} , it was derived from the telescopic vibrations of Fe-O bond in the tetrahedral positions [46]. Remarkably, all the above characteristic peaks of CNQDs and $\text{C}_1\text{F}_1\text{O}$ could be detected in the $1.0\text{CNQDs}@ \text{C}_1\text{F}_1\text{O}$ hybrid, confirming the successful combination of CNQDs and $\text{C}_1\text{F}_1\text{O}$. The broad band in the $3100\text{--}3500\text{ cm}^{-1}$ region as well as the peaks at 2855 and

2920 cm^{-1} were associated to the stretching vibration of the N-H bond in amino groups or water molecules, respectively [47].

In order to analyze the specific surface areas and pore radius information of the synthesized materials, N_2 adsorption-desorption tests were further conducted. As depicted in Fig. 2d, the isotherm curves for all samples were manifested as typical type-IV, suggesting the mesoporous features of the prepared photocatalysts. The specific surface areas and pore structure parameters of $1.0\text{CNQDs}@ \text{C}_1\text{F}_1\text{O}$ as well as the unmodified CFO with various Fe/Cu molar ratios were summarized in Fig. 2f and Table S1. Clearly, the value of the specific surface area of $\text{C}_1\text{F}_1\text{O}$ ($84.37\text{ m}^2\text{ g}^{-1}$) was much higher than those of $\text{C}_1\text{F}_4\text{O}$ ($67.03\text{ m}^2\text{ g}^{-1}$) and $\text{C}_4\text{F}_1\text{O}$ ($59.49\text{ m}^2\text{ g}^{-1}$). The main reason for this was that the surface of $\text{C}_1\text{F}_1\text{O}$ hollow microspheres had a unique gully-like structure formed by particle accumulation, which made its roughness more obvious than other photocatalysts as verified by SEM results. In the case of $1.0\text{CNQDs}@ \text{C}_1\text{F}_1\text{O}$ ($98.51\text{ m}^2\text{ g}^{-1}$), a slight increase in the specific surface area was due to the change of surface roughness by the loaded CNQDs. At the same time, the mean pore size of $1.0\text{CNQDs}@ \text{C}_1\text{F}_1\text{O}$ compared with $\text{C}_1\text{F}_1\text{O}$ was down from 12.94 to 9.18 nm (Fig. 2e), suggesting that CNQDs occupied some pore space of $\text{C}_1\text{F}_1\text{O}$.

3.2. Photoelectrochemical and optical properties

To explore the interfacial electron transfer behaviors of the prepared materials, photoelectrochemical measurements, PL, and TRPL spectra were measured. As depicted in Fig. 3a, the rapid and intermittent photocurrent signals appeared in the cycles of the switching light source system. Compared with the bare $\text{C}_1\text{F}_1\text{O}$ sample, the photocurrent density of $1.0\text{CNQDs}@ \text{C}_1\text{F}_1\text{O}$ was stronger, meaning the superior carriers migration capability. Normally, the size of Nyquist semicircle is in direct proportion to the charge transfer resistance on the electrode coated with sample [16]. As expected, the much smaller arc radius of $1.0\text{CNQDs}@ \text{C}_1\text{F}_1\text{O}$ demonstrated a massive decline in impedance value in contrast to the unmodified materials (Fig. 3b). Based on the equivalent circuit diagram of EIS (inset in Fig. 3b), the fitted charge transfer resistance (R_{ct}), solution resistance (R_{ct}), and CPE_{dl} (electrochemical double-layer capacitance) for all tested samples are listed in Table S2, and the lower R_{ct} values for $1.0\text{CNQDs}@ \text{C}_1\text{F}_1\text{O}$ and used $1.0\text{CNQDs}@ \text{C}_1\text{F}_1\text{O}$ confirmed their better interfacial charge transfer

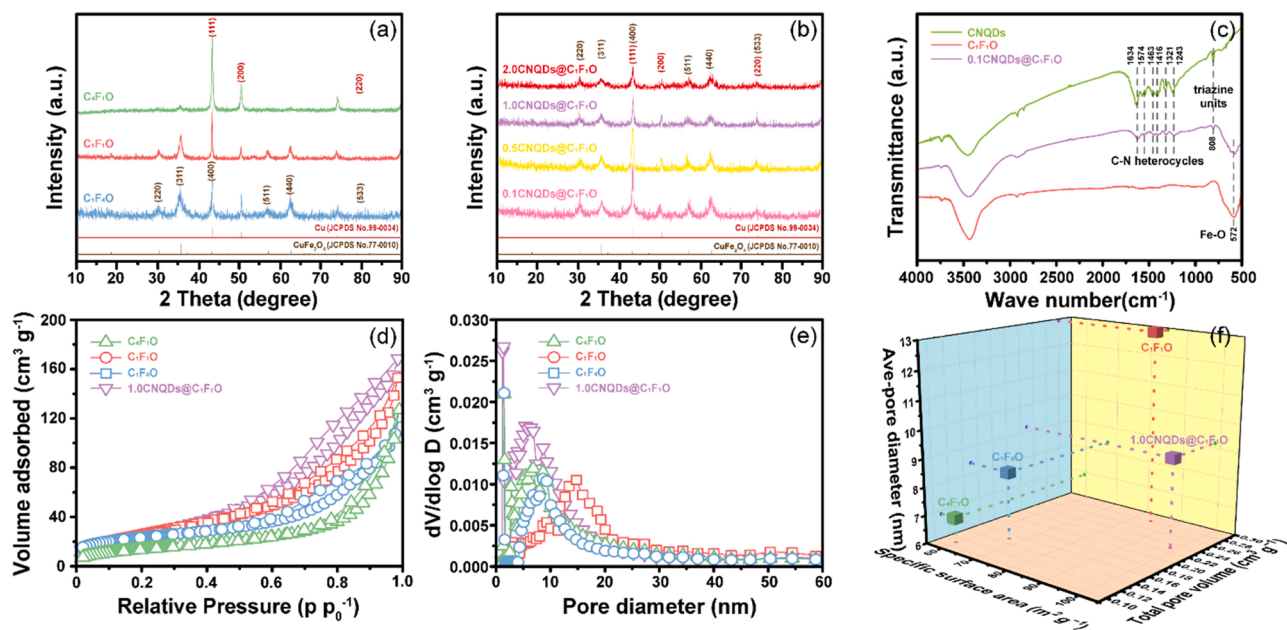


Fig. 2. (a and b) XRD patterns, (c) FTIR spectra, (d) N_2 adsorption-desorption isotherms, (e) pore size distribution curves, and (f) the detailed specific surface areas and pore structure parameters of the synthesized samples.

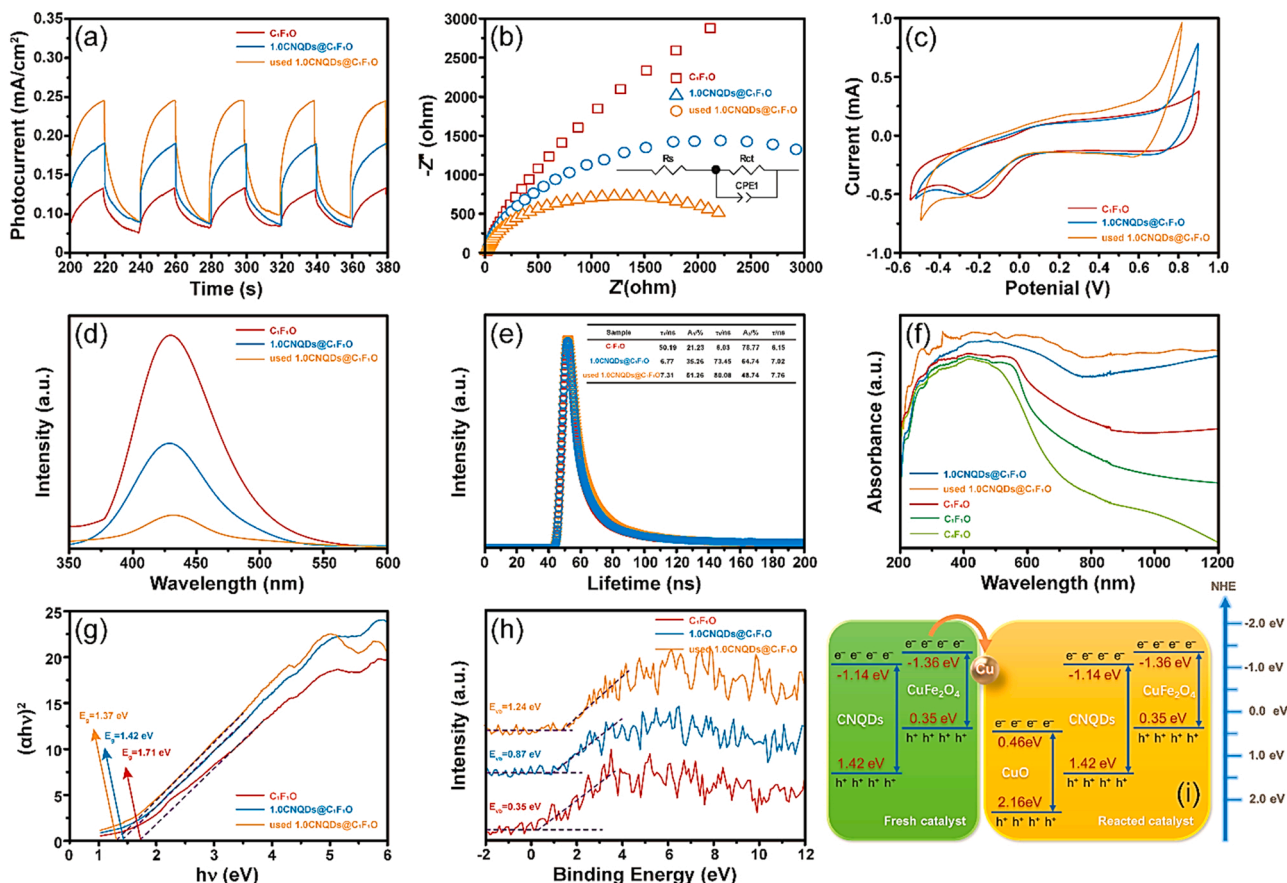


Fig. 3. The photoelectrochemical and electronic structure characterization of the prepared materials. (a) Photocurrent-time (i-t) curves, (b) EIS Nyquist plots (inset: equivalent circuit diagram), (c) CV profiles, (d) PL spectra, (e) the fitted TRPL curves, (f) UV-vis DRS spectra, (g) the corresponding Tauc's plots, (h) VB-XPS spectra, and (i) schematic band alignment.

efficiencies. Meanwhile, it was clearly observed that the CV profile of 1.0CNQDs@C₁F₁O enclosed a larger loop with higher photocurrent density relative to C₁F₁O (Fig. 3c), which was consistent with the results of photocurrent-time curves and EIS Nyquist plots. Therefore, the incorporating of CNQDs, CuFe₂O₄, and Cu⁰ did solve the default of easy recombination of photoexcited electrons and holes. Besides, it was a remarkable fact that the photoelectrochemical properties of the used 1.0CNQDs@C₁F₁O was even better than that of the fresh sample. This was mainly because Cu⁰ in the 1.0CNQDs@C₁F₁O photocatalyst was converted into CuO during the PMS activation reaction, and the formed heterojunctions between CuO, CNQDs, and C₁F₁O could further ensure effective electron/hole separation.

PL technology was further employed to clarify the transfer dynamics of photogenerated carriers in the C₁F₁O, 1.0CNQDs@C₁F₁O, and used 1.0CNQDs@C₁F₁O samples. A weaker strength of PL emission peak implies a lower recombination rate of photoexcited electrons and holes because the PL signals stem from the energy released by carrier recombination [46]. From Fig. 3d, the pristine C₁F₁O possessed a more apparent emission peak as compared to 1.0CNQDs@C₁F₁O composite, showing once again that the problem of the rapid electron and hole recombination over C₁F₁O was alleviated indeed by coupling with CNQDs. For a deeper understanding the charge separation dynamics behavior, TRPL decay spectra were then utilized to measure the lifetime of photogenerated electrons (Fig. 3e). The average emission lifetimes (τ) of the photocatalysts prior and post to modification were 6.15 ns ($\tau_1 = 50.19$ ns, $A_1 = 21.23$ %; $\tau_2 = 6.03$ ns, $A_2 = 78.77$ %) and 7.02 ns ($\tau_1 = 6.77$ ns, $A_1 = 35.26$ %; $\tau_2 = 73.45$ ns, $A_2 = 64.74$ %), respectively. Accordingly, a conclusion could be drawn that the introduction of CNQDs on the C₁F₁O surface was beneficial to increase carrier

availability and lifetime. Evidently, due to the establishment of new CuO/CNQDs/C₁F₁O nanojunction structure, the used material had higher electron separation efficiency and longer fluorescent lifetime than that of C₁F₁O and 1.0CNQDs@C₁F₁O, which was following the photoelectrochemical test results.

Next, to study the optical utilization level of the obtained samples, UV-vis DRS spectra was executed. For the CFO prepared with various ratios of precursors (Fig. 3f), the absorption edge appeared substantial red-shift and the corresponding light harvesting capacity was also improved with the increase of Fe content in the photocatalyst. After introducing CNQDs, the 1.0CNQDs@C₁F₁O hybrid presented intense response in the visible and near-infrared region, with a further red-shifted absorption threshold, which could be ascribed to the preeminent quantum confinement effect and up-conversion photoluminescence performance of CNQDs. Notably, compared with the fresh material, although the used 1.0CNQDs@C₁F₁O sample possessed similar optical absorption intensity over the wavelength range of 200–1200 nm, its absorption edge undergone some changes, implying the altered structural composition of photocatalyst in the process of PMS-assisted oxidation degradation reaction. To prove that assertion, the Tauc's plot derived from the DRS spectra was plotted for probing the variations of band gap energy (E_g). As revealed in Fig. 3g, the E_g values of C₁F₁O, 1.0CNQDs@C₁F₁O, and used 1.0CNQDs@C₁F₁O were measured to be 1.71, 1.42, and 1.37 eV, respectively. The further narrowed E_g for the spent material might arise from the formation of new component on the basis of the original sample.

More studies have been done for grasping the electronic band structure of these samples, the valance band potential (E_{VB}) of C₁F₁O, 1.0CNQDs@C₁F₁O, and used 1.0CNQDs@C₁F₁O were 0.35, 0.87, and

1.24 eV, respectively, estimated by the VB-XPS spectra (Fig. 3h). The increased E_{VB} was likely the result of the modification of CNQDs and the conversion of Cu^0 to CuO during the PMS-photocatalysis process. Accordingly, the conduction band potential (E_{CB}) of these photocatalysts could be figured out by the equation of $E_{CB} = E_{VB} - E_g$. Therefore, the E_{CB} of C_1F_1O , $1.0CNQDs@C_1F_1O$, and used $1.0CNQDs@C_1F_1O$ were calculated as -1.36 , -0.55 , and -0.13 eV for each. Furthermore, based on the computational band gap information of CNQDs (Fig. S3) and CuO acquired from other reports [48,49], the electron configurations of the fresh and used photocatalyst were schematically illustrated in Fig. 3i. From these results we could deduce that the well-matched p-n-p heterojunction structure was constructed among CNQDs, CuO and $CuFe_2O_4$ in the reacted sample, which would further promote the carriers interface movement and extended their lifetime, contributing to the efficient conversion of photon energy in photocatalyst.

3.3. Photocatalytic activity

A series of control experiments were executed to study the photocatalytic activities of the fabricated materials towards 5-FLU in the visible-light-driven PMS-photocatalysis system. The removal profile in the existence of CFO samples with various proportions of Fe and Cu were displayed in Fig. 4a. The result found that C_1F_1O had the highest photocatalytic oxidation ability, which might be attributed to that the rough gully-like structure formed by the accumulation of nanoparticles increased the active sites and the reasonable composition proportion of $CuFe_2O_4$ and Cu^0 in composite promoted PMS activation and photocatalytic reaction. Although the higher content of Cu^0 in C_4F_1O was conducive to activate PMS at the beginning of the reaction, the

degradation rate became slow at the middle and late stages, which mainly resulted from the poor photocatalytic performance of C_4F_1O . All the $CNQDs@C_1F_1O$ composites performed superiorly over the bare C_1F_1O (Fig. 4b), indicating that the photoconversion efficiency and catalytic properties improved by the synergistic effect between components. Notably, as the loading amount of CNQDs grew in $0.1CNQDs@C_1F_1O$ to $1.0CNQDs@C_1F_1O$, the photocatalytic activity was incrementally ascended; but when its content further raised from $1.0CNQDs@C_1F_1O$ to 2.0% $CNQDs@C_1F_1O$, the degradation performance was then descended. The above findings could be explained by that the excessive loading of CNQDs caused a shading effect, resulting in the decline in photocatalytic properties. Given the best PMS-assisted photocatalytic behavior of $1.0CNQDs@C_1F_1O$, the 1.0 % loading amount was chosen for the follow-up experiments.

To determine the synergistic effect of various parts in the coupling system, the contributions of $1.0CNQDs@C_1F_1O$, visible light as well as PMS to 5-FLU decomposition were compared in Fig. 4c. Plainly, the structure of 5-FLU was quite stable, and its degradation could be negligible only under visible light. Even if both visible light and PMS existed at the same time, the purification performance was also not satisfactory, implying that visible light cannot effectively activate PMS. By contrast, the heterogeneous PMS oxidation process ($1.0CNQDs@C_1F_1O/PMS$) and photocatalysis system ($1.0CNQDs@C_1F_1O/vis$) led to 5-FLU removal efficiencies of 42.3 % and 63.1 %, respectively. Significantly, a considerable improvement in the elimination of 5-FLU were observed in the $1.0CNQDs@C_1F_1O/PMS/vis$ system, where an unprecedented 99.4 % removal efficiency could be achieved in the same time period, suggesting the existence of synergetic promotion effect in the studied PMS-photocatalysis system. As profiled

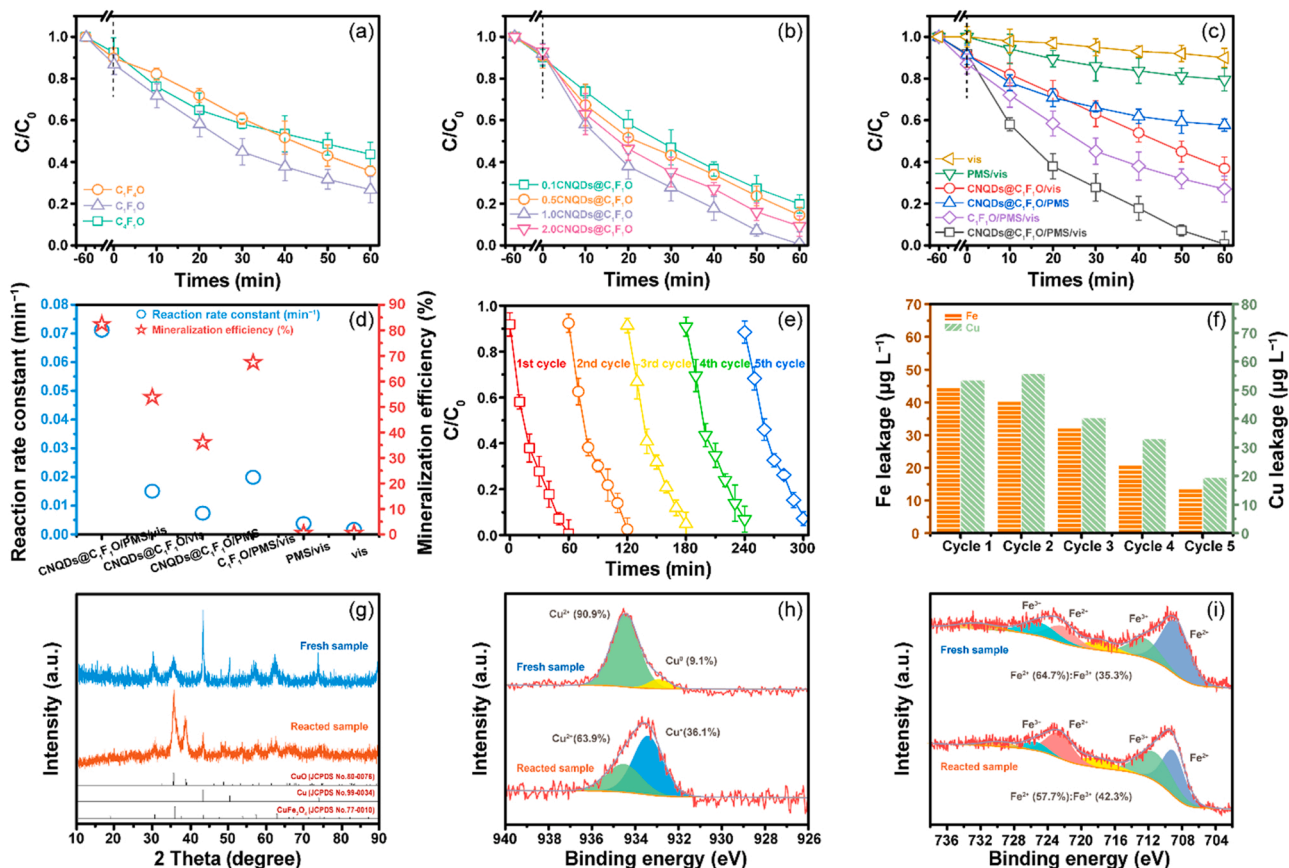


Fig. 4. Comparison of 5-FLU removal in (a) CFO samples with various Cu and Fe proportions, (b) $CNQDs@C_1F_1O$ samples with various CNQDs loadings, and (c) different oxidation systems. (d) The corresponding reaction rate constant and TOC removal efficiency. (e) Cycling runs for the photocatalytic decomposition of 5-FLU in the $1.0CNQDs@C_1F_1O/PMS/vis$ system. (f) Fe and Cu leakages of synthesized $1.0CNQDs@C_1F_1O$ composite. (g) XRD spectra, and high-resolution (h) Cu 2p and (i) Fe 2p XPS spectra of the fresh and reacted $1.0CNQDs@C_1F_1O$ samples. (Conditions: 30 μM 5-FLU, 0.2 $g L^{-1}$ catalyst, 0.3 mM PMS, pH = 6.4, and 25 $^{\circ}C$).

by Fig. 4d, the 5-FLU degradation rate in different systems conformed to the pseudo-first-order kinetic equation ($\ln(C/C_0)$ vs. time). The observed reaction rate constant (k) value of 1.0CNQDs@C₁F₁O/PMS/vis system (0.0711 min^{-1}) was much faster than that of the systems of 1.0CNQDs@C₁F₁O/PMS (0.0074 min^{-1}) and 1.0CNQDs@C₁F₁O/vis (0.0151 min^{-1}). It was further proof of the collaborative processes between visible-light driven photocatalysis and PMS activation during purifying polluted water. Noticeably, a better performance in 5-FLU mineralization also could be achieved in the 1.0CNQDs@C₁F₁O/PMS/vis system.

To explore the actual application possibility of photocatalyst, the cycling stability of sample was appraised (Fig. 4e). Specifically, the magnetic powder material could be easily gathered by external magnetic field after each degradation experiment, followed by thorough rinsing and drying, and finally calcined in a reducing atmosphere for the next round of photocatalytic process. Impressively, the prepared 1.0CNQDs@C₁F₁O composite showed satisfactory reusability and reliability, and over 92.6 % of 5-FLU was degraded after five consecutive recycling runs. The slight decrease in degradation efficiency was mainly due to the loss of catalyst during recovery and the shielding of active sites by residual intermediates adsorbed on the catalyst surface. Interestingly, in the process of the repeated catalytic degradation, Fig. 4f shown that the synthesized 1.0CNQDs@C₁F₁O composite displayed fairly low metal leakage ($\text{Fe} \leq 44.7 \mu\text{g L}^{-1}$, $\text{Cu} \leq 53.5 \mu\text{g L}^{-1}$), which was far less than the standard for surface water quality (GB3838–2002). This result facilitated the practical use of the photocatalyst as it would reduce the harm of serious heavy metal pollution.

The magnetic properties of the synthesized C₁F₁O and 1.0CNQDs@C₁F₁O materials were measured by VSM at room temperature (Fig. S4). The magnetization saturation of C₁F₁O was found to be 25.73 emu g^{-1} and dropped to 23.29 emu g^{-1} when the C₁F₁O was coated with 1.0 % CNQD, suggesting that the non-magnetic CNQD as the co-catalyst had not virtually affect the magnetic behavior of C₁F₁O. Consequently, under an external magnetic field, 1.0CNQDs@C₁F₁O could be employed as a recyclable material for the treatment of organic wastewater, verifying its practical future. In addition, the used 1.0CNQDs@C₁F₁O composite were characterized by XRD, SEM, TEM, and XPS to study the changes of its structure, morphology, composition, and valence state before and after PMS-photocatalytic reaction. Comparing the XRD patterns of the fresh and reacted samples (Fig. 4g), Cu⁰ in the composite would gradually be converted into CuO, while the CuFe₂O₄ phase could remained stable. The morphology of material became rougher after the degradation of 5-FLU, which could be explained by the formation of CuO on the 1.0CNQDs@C₁F₁O surface (Fig. S5). Moreover, from the TEM images (Fig. S6), the hollow structure of the reacted 1.0CNQDs@C₁F₁O could be well retained, and the (110) plane of CuO was also appeared, with the interplanar distance of 0.275 nm.

As shown in Fig. 4h, the high-resolution Cu 2p spectrum of the fresh sample presented two peaks at 932.8 and 934.6 eV, which could be indexed to Cu⁰ and Cu²⁺, respectively. After activating PMS, the peak of Cu⁰ disappeared, replaced by Cu⁺, and the mass percent of Cu⁺ and Cu²⁺ was 63.9 % and 36.1 %, respectively. This result further confirmed the structural evolution of photocatalyst during the catalytic process, consistent with the XRD and HRTEM results. Fig. 4i depicted the core-level regions of Fe 2p, which could be split into six peaks, and the binding energies at 710.3 and 723.1 eV were ascribed to Fe²⁺ and at 711.2 and 725.4 eV were assigned to Fe³⁺, respectively. In comparison with the fresh sample, the spent photocatalyst had the same peak location, but the relative content of Fe²⁺ declined from 64.7 % to 57.7 %, suggesting that Fe²⁺ served as the main active centers on the 1.0CNQDs@C₁F₁O surface to activate PMS. Besides, in the studied PMS-photocatalysis system, the rebirth cycle of Fe²⁺/Fe³⁺ could be promoted with assistance of Cu species and photogenerated electrons, thus ensuring the reusability of the prepared composite. As for O element in the samples before and after reaction, similar patterns could be seen in

the fitted O 1s spectra, two peaks at 528.6 and 530.8 eV corresponded to the surface lattice oxygen and adsorbed oxygen (Fig. S7)[32]. From the results in Fig. S8 and S9, it was clear that the high resolution XPS spectra of C 1s and N 1s had not changed much, which proved the CNQDs were well preserved in the photocatalyst. Meanwhile, the regenerated material was characterized by XPS and XRD. The analysis results in Fig. S10 showed that the composition and structure of the reacted catalyst could be well recovered after being calcined in a H₂-reducing atmosphere.

In the natural aquatic environment, several coexisting substances including inorganic anions and natural organic matter are ubiquitous, which will inevitably interfere with the degradation process dominated by free radicals. Consequently, humic acid (HA), Cl[−], CO₃^{2−}, and HPO₄^{2−} as representative were added into the PMS-photocatalysis system at different concentrations to assess their influence on the oxidation decomposition of target pollutant. From Fig. 5a–d, it was found that under the background of Cl[−], CO₃^{2−}, HPO₄^{2−}, and HA, as the concentration of these additives continued to increase, the corresponding degradation efficiencies of 5-FLU showed different degrees of change. The results revealed that the order of suppressing the 5-FLU degradation follows that of HA > HPO₄^{2−} > CO₃^{2−} > Cl[−] under the optimal reaction condition. Specifically, when the concentration of Cl[−] raised from 5 to 20 mM, no significant change in the attenuation curve, indicating that the inhibition of Cl[−] on the 1.0CNQDs@C₁F₁O/PMS/vis system could be ignored (Fig. 5a). This was principally because of the production of intermediate Cl[•] through the reaction between SO₄^{•−} and Cl[−] in the catalytic oxidation process [50]. In the case of CO₃^{2−}, as its concentration increased, the oxidation degradation of 5-FLU was limited to a certain level (Fig. 5b). Such a phenomenon might be attributed to the capture of SO₄^{•−} and [•]OH by CO₃^{2−} to generate comparatively weak CO₃^{•−} ($E^0 = 1.78 \text{ V}$) [51]. However, as displayed in Fig. 5c, HPO₄^{2−} exerted a great impact on the 5-FLU decay with a 20.7 % reduction in degradation efficiency, which might be related to the quenching effect and strong affinity of HPO₄^{2−}. It can be observed from Fig. 5d that the repression of low dose of HA on the oxidation degradation of 5-FLU was unobvious, while excess HA had a marked inhibitory effect on the removal performance of the coupling system, which was mainly caused by the competition between HA and 5-FLU for the active sites on the 1.0CNQDs@C₁F₁O surface.

For photocatalysis and PMS activation process, the pH of solution is an important parameter, thereby a comparative study on the degradation efficiency of the original reaction with conditions at different pH values was conducted. As depicted in Fig. 5e, the pH of the original reaction was measured to be 6.4, corresponding to a removal efficiency of 99.4 %. On the whole, the degradation efficiency of 5-FLU increased with the increase of initial pH value. Under acid environment, the combination of H⁺ with HSO₅[−] was dominant, which reduced the oxidation performance of the coupling system. Meanwhile, the deteriorated degradation efficiency might also be the result of excessive H⁺ consuming ROS like SO₄^{•−} and [•]OH. In alkaline condition, OH[−] could involve in the decomposition of PMS, thus accelerating the production of ROS. The stability of the 1.0CNQDs@C₁F₁O composite at different pHs was investigated by XRD and FTIR analysis. As can be seen from the Fig. S11a, C₁F₁O could remain stable in the pH range of 3–11 without obvious structural changes. Moreover, the feature peaks of CNQDs and CFOs can be clearly observed from the FTIR spectra of the 1.0CNQDs@C₁F₁O in highly acidic/alkaline range (Fig. S11b), confirming the stability of the combination of CNQDs and C₁F₁O. To evaluate the performance of the 1.0CNQDs@C₁F₁O/PMS/vis system for pharmaceuticals removal in actual water bodies, tap water, surface water collected from Songshan Lake, and secondary effluent sampled in a sewage treatment plant (their basic properties see Table S3), after being filtered, were used to prepare the 5-FLU solution for photo-degradation experiment. As can be seen from the Fig. 5f, compared to the deionized water, the catalytic behavior of the optimal photocatalyst were retarded slightly in different water matrixes, with less than 7.6 % reduction in the degradation efficiency, signifying the ingenious

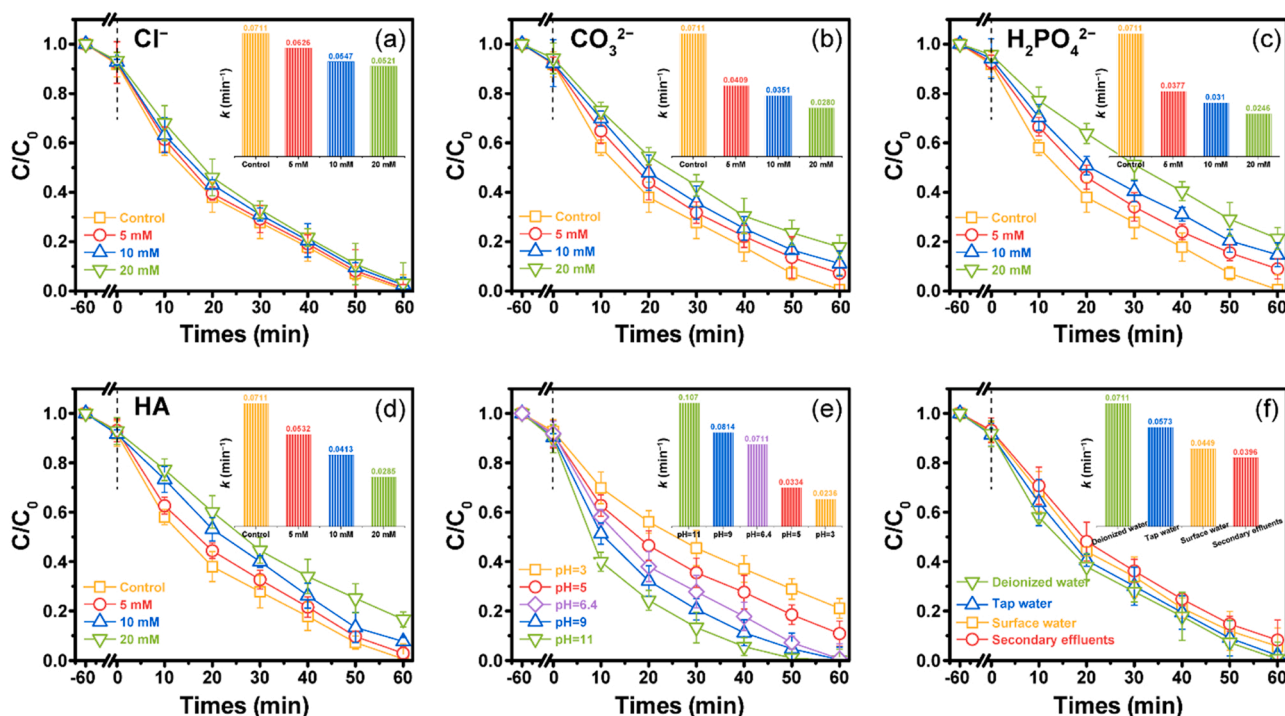


Fig. 5. The influences of the coexisting substances, such as (a) Cl^- , (b) CO_3^{2-} , (c) HPO_4^{2-} , (d) HA, as well as (e) initial solution pH and (f) water matrix on the 5-FUL degradation in the 1.0CNQDs@C₁F₁O/PMS/vis system. (Conditions: 30 μM 5-FUL, 0.2 g L⁻¹ catalyst, 0.3 mM PMS, pH = 6.4 for a–d and f, and 25 °C).

adaptability of the obtained material in practical application.

The effect of PMS concentration, catalyst dosage, and temperature on the removal of 5-FUL was further studied. Fig. S12a shows the influence of PMS concentration (0.1, 0.3, 0.5, and 1.0 μM) on 5-FUL removal rate. Apparently, the degradation of 5-FUL was markedly enhanced by elevating PMS concentration, and reached 100 % in less time, which can be explained by the fact that increasing PMS concentration would generate more radicals to accelerate the oxidative decomposition of 5-FUL. A similar phenomenon was also seen for the catalyst dosage (Fig. S12b), demonstrating that increasing catalyst dosage had a positive effect on 5-FUL degradation. This result can be ascribed to more active and adsorption sites being provided at appropriately higher catalyst dosages. As revealed in Fig. S12c, with the increase of temperature from 25 to 45 °C, the removal efficiency of 5-FUL in the 1.0CNQDs@C₁F₁O/PMS/vis system gradually increased. This was because high temperature facilitated PMS molecules to overcome activation energy barrier and accelerated the diffusion of 5-FUL and PMS molecules.

A comparative study with other catalyst/oxidant systems was performed in Fig. S13, from which it can be seen that the 1.0CNQDs@C₁F₁O/PMS/vis system showed more excellent performance for degrading and mineralizing 5-FUL in a shorter reaction time than many previous studies. Besides, the application of these reported strategies like UV photolysis [52], photocatalysis with Degussa P25 [53], ozonation [11], electrolysis [6], Fenton-like process [8], and electro/photo-Fenton process [12,13,54] was commonly limited by the drawbacks of long processing time, high treatment costs, sluggish metal ions redox cycle, secondary metal-rich sludge pollution, narrow operation pH range, and inconvenient catalyst recovery. The newly-developed relay oxidation system in this study can effectively avoid or alleviate the above problems, further highlighting its superiority.

3.4. Catalyst optical parameters

It is well known that the photocatalytic activity depends strongly on the rate of photon absorption in the reactor and this varies with catalyst concentration and with catalyst specimens. Therefore, the optical

properties of the papered photocatalyst were investigated by determining their optical parameters, including local volumetric rate of photon absorption (LVRPA), total rate of photon absorption (TRPA), and combined parameter the optical thickness (τ_{app}). According to the Eqs. (1)–(17) (detailed explanation and definition of these equations and parameters on the optical properties of catalyst were described in the previous literature [39–43]), the absorption (κ^*), scattering (σ^*), and extinction (β^*) coefficient of the obtained samples were summarized in Table 1. Moreover, the catalyst concentration dependent TRPA/A profile was plotted in Fig. 6a, which could provide a better understanding for the applicability of the synthesized materials in photocatalytic degradation. Obviously, the curves of TRPA/A gradually increased with increase in catalyst concentration until they approached plateaus. The region where the loading of catalyst corresponding to TRPA/A reaching a constant value (less than 5 % change) was thought to be an optimal value. For 1.0CNQDs@C₁F₁O, such optimum value was calculated at around 0.2 g L⁻¹, corresponding to an τ_{app} of 7.94.

In order to make a fair comparison between the different catalysts, the photocatalytic degradation experiments were performed at equal τ_{app} value. As displayed in Table 2, the τ_{app} values for all the materials demonstrated an increasing tendency with the increase in the concentration of catalysts. Moreover, by matching with the Table 2, it can be found that when the τ_{app} was fixed at 7.8–8.2 (optimum value for 1.0CNQDs@C₁F₁O), the corresponding concentrations for each catalyst were approximately around 0.2–0.3 g L⁻¹. Specifically, as shown in

Table 1
Optical parameters of the photocatalyst.

Materials	β^* (m ² kg ⁻¹)	κ^* (m ² kg ⁻¹)	σ^* (m ² kg ⁻¹)
C ₁ F ₄ O	480.7	188.5	292.2
C ₁ F ₁ O	489.9	164.3	325.6
C ₄ F ₁ O	477.7	176.5	301.2
0.1CNQDs@C ₁ F ₁ O	493.1	152.6	340.5
0.5CNQDs@C ₁ F ₁ O	508.4	158.2	350.2
1.0CNQDs@C ₁ F ₁ O	511.8	161.9	349.9
2.0CNQDs@C ₁ F ₁ O	509.6	160.7	348.9

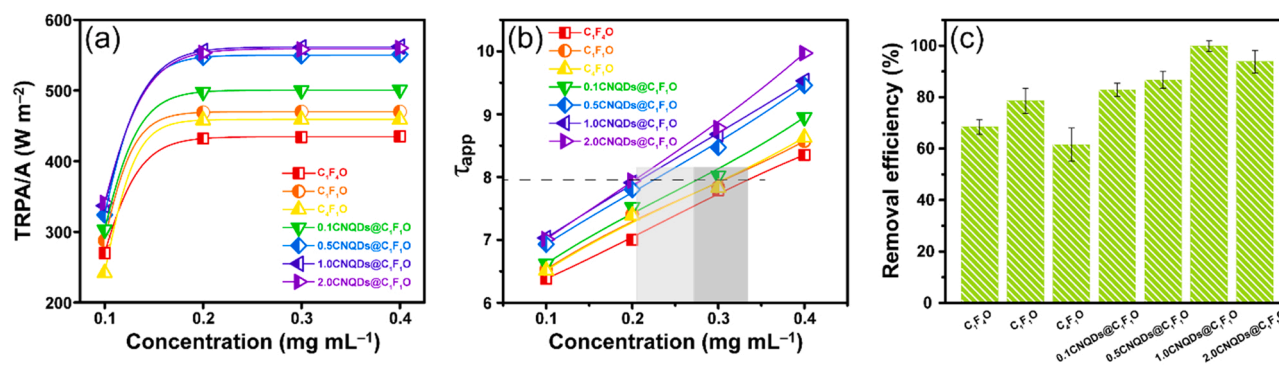


Fig. 6. (a) Photocatalyst concentration dependent TRPA/A profile. (b) Photocatalyst concentration dependent optical thickness profile. (c) Photocatalytic degradation experiments at equal optical thickness. (Conditions: 30 μ M 5-FLU, 0.3 mM PMS, pH = 6.4, and 25 $^{\circ}$ C).

Table 2
Photocatalyst concentration dependent optical thickness.

Concentration (g L ⁻¹)	0.1	0.2	0.3	0.4
C ₁ F ₄ O	6.38	7.00	7.79	8.35
C ₁ F ₁ O	6.53	7.41	7.84	8.57
C ₄ F ₁ O	6.51	7.39	7.83	8.63
0.1CNQDs@C ₁ F ₁ O	6.62	7.52	8.02	8.95
0.5CNQDs@C ₁ F ₁ O	6.93	7.80	8.47	9.46
1.0CNQDs@C ₁ F ₁ O	7.01	7.94	8.78	9.97
2.0CNQDs@C ₁ F ₁ O	7.03	7.91	8.68	9.53

Fig. 6b, the concentrations of C₁F₄O, C₁F₁O, C₄F₁O, 0.1CNQDs@C₁F₁O, 0.5CNQDs@C₁F₁O, 1.0CNQDs@C₁F₁O, and 2.0CNQDs@C₁F₁O catalysts were ca. 0.33, 0.31, 0.31, 0.27, 0.23, 0.21, and 0.21 g L⁻¹ at the τ_{app} value of 7.94, respectively. Fig. 6c displayed the 5-FLU degradation effects of different catalysts at equal τ_{app} value. It can be observed that 1.0CNQDs@C₁F₁O had the best removal efficiency in 60 min of irradiation, which agreed well with the experimental results in Fig. 4a and b.

3.5. Identification of degradation intermediates

To reveal the decomposition pathways of 5-FLU in the studied coupling oxidation system, the reaction solution sampled at different treatment periods, were analyzed using UPLC-MS/MS technique. A total of fourteen intermediates were identified in the mass spectra acquired over a range from 20 to 500 m/z with a positive ionization mode (Fig. S14) and their details, i.e., chemical structure, molecular formula, and m/z data, are summarized in Table S4. In the light of the detected characteristic fragments as well as recent relevant studies [4,55], the plausible transformation routes were speculated, primarily involving in hydroxylation, hydrogenation, defluorination, and ring-opening processes, as depicted in Fig. 7a.

In pathway I, the degradation of 5-FLU was occurred via hydrogenation and subsequent addition of hydroxyl group on the aromatic ring to form TP1 ($m/z = 148$). Then the loss of fluorine atom for this compound could produce TP2 ($m/z = 128$) with an enol form structure, and it would come to a balance with its keto tautomer TP3 ($m/z = 128$). These formed metabolites could be further hydroxylated to yield dihydroxylated and trihydroxylated fragments, named as TP4 ($m/z = 144$) and TP5 ($m/z = 160$), respectively. After consecutive multiple hydroxylation steps, the carboxylic acid derivative TP6 ($m/z = 162$) was obtained as the ring-opening product. In pathway II, a single hydroxylation reaction was assumed to be an essential step in the initial stages of 5-FLU removal, giving rise to TP9 ($m/z = 146$) and TP10 ($m/z = 146$). Above hydroxylated compounds could experience defluorination process caused by ROS attack on the C-F bond on the one hand, resulting in TP2 and TP3, on the other hand be directly oxidized to cleave its aromatic ring and converted to TP11 ($m/z = 162$). Moreover, the release of some

smaller molecular were also found, such as TP7 ($m/z = 89$), TP8 ($m/z = 89$), TP12 ($m/z = 106$), TP13 ($m/z = 62$) and TP14 ($m/z = 60$), which derived from the deep oxidation of the found byproducts, and they would continue to breakdown into harmless inorganic substances finally.

To further assess the efficacy of the CNQDs@CFO/PMS/vis system for degrading 5-FLU, the acute (LC50 and EC50) and chronic toxicity (Chv) of 5-FLU and its intermediates to fish, daphnia and green algae were calculated according to the ecological structure activity relationships (ECOSAR). From the ECOSAR analysis (Fig. 7b and c, Table S5), the LC50 and EC50 values of 5-FLU to fish, daphnid, and green algae were 818, 281 and 0.0093 mg L⁻¹, respectively. And the Chv values of 5-FLU to the above-mentioned organisms were predicted to be 4.25, 87.5 and 0.0026 mg L⁻¹, respectively. Clearly, these data illustrated that the target compound 5-FLU could be indexed to very toxic level. While for the most of degradation products, both their acute and chronic toxicity presented a falling tendency due to the continuous attack of ROS. Although some intermediates (TP1, TP3, TP10, and TP13) were classified as very toxic, their EC50 and Chv values for green algae were still lower than that of 5-FLU in different degrees. Moreover, these toxic byproducts could be broken down continuously in the relay oxidation process, which was gratifying. By and large, the final decomposition products of 5-FLU in the CNQDs@CFO/PMS/vis system were low toxic or even non-toxic after 60 min of PMS-photocatalytic treatment, alleviating the harm to the ecological environment.

3.6. PMS accelerating photodegradation mechanism

The electron migration among photocatalyst, oxidant, and pollutant was explored to elucidate the synergistic degradation mechanism of the PMS-photocatalysis coupling system. As evidenced by the $i-t$ curves in Fig. 8a, the current density was distinctly changed after introducing PMS, attributable to the formation of a metastable intermediate (1.0CNQDs@C₁F₁O-PMS*) through charge transfer from photocatalyst to PMS [56]. Besides, the addition of 5-FLU gave rise to another increment in current density, which might be caused by the decomposition of PMS* into ROS to attack pollutant molecules. Notably, this phenomenon was more obvious in the 1.0CNQDs@C₁F₁O/PMS/vis system compared with the C₁F₁O/PMS/vis system, indicating the excellent PMS activation and photocatalytic ability of 1.0CNQDs@C₁F₁O. Fig. 8b manifests that the dissolved O₂ played a positive role on 5-FLU removal in the 1.0CNQDs@C₁F₁O/PMS/vis system. The reaction rate was accelerated essentially in the O₂-saturated system, and 5-FLU could be completely removed within 50 min of irradiation. In contrast, when the dissolved O₂ in the reaction solution was purged out by N₂, merely 53.2 % of 5-FLU was eliminated over the identical timeline. The above result confirmed that the dissolved O₂ could involve in the evolution of free radicals and facilitate the formation of ROS.

To analyze the contributions of the ROS generated in the

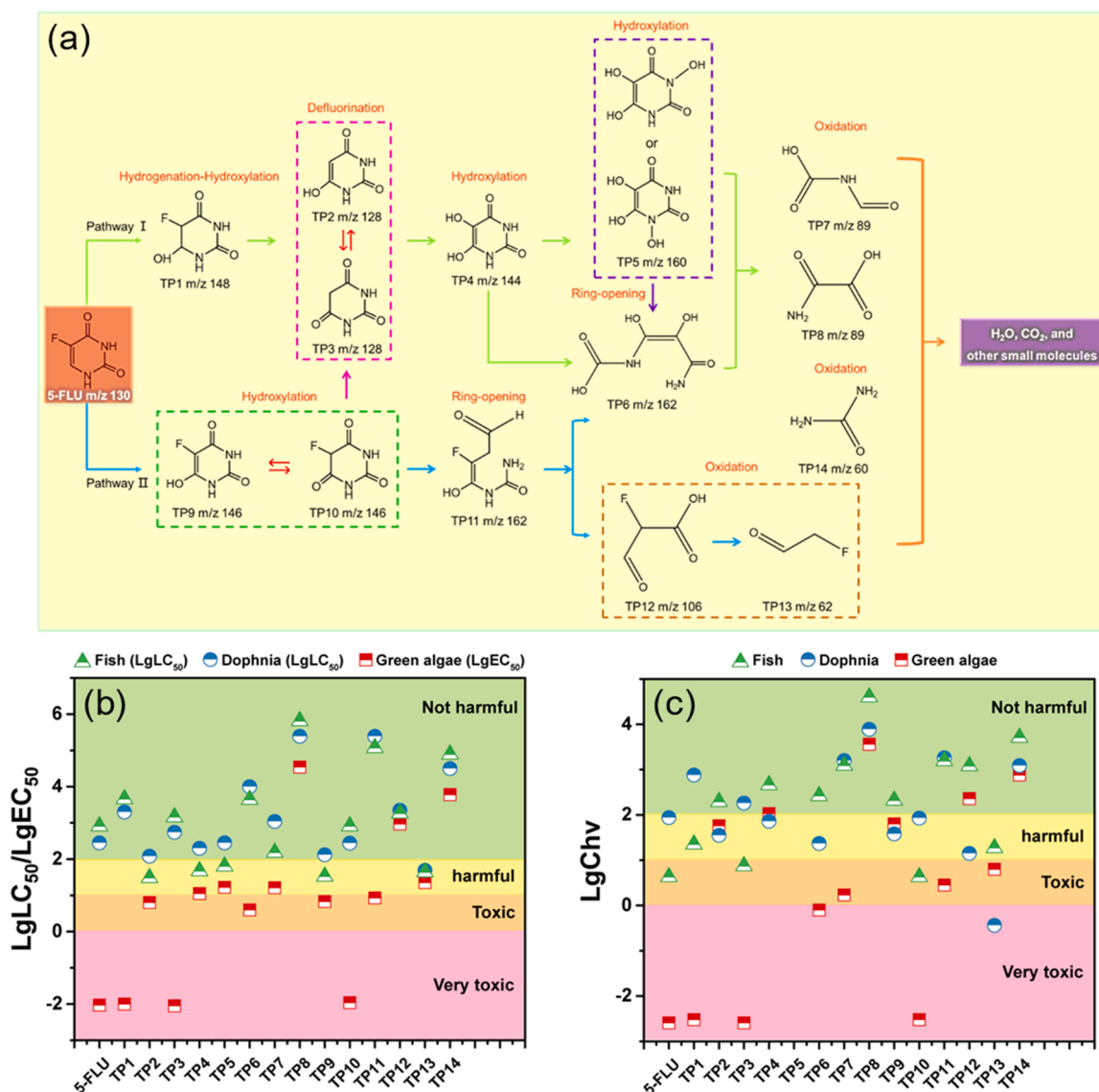


Fig. 7. (a) Decomposition pathways of 5-FLU in the studied PMS-photocatalysis system. (b) Predicted acute toxicity and (c) chronic toxicity of 5-FLU and its intermediates by ECOSAR program.

1.0CNQDs@C₁F₁O/PMS/vis system to the 5-FLU removal, a series of radical quenching experiments and EPR measurements were performed. Methanol (MeOH) was used as a mighty scavenger for capturing both $\bullet\text{OH}$ and $\text{SO}_4^{\bullet-}$, and isopropyl alcohol (IPA), L-carnosine (L-car), L-histidine (L-his), and ammonium oxalate (AO) were suitable probe for $\bullet\text{OH}$, $\text{O}_2^{\bullet-}$, $^1\text{O}_2$, and holes, respectively. As described in Fig. S15, in the early stage of the reaction, the restraining action of MeOH was greater relative to other quenchers, while the quenching performance of IPA and AO became more prominent in the later stage of the reaction. The results inferred that $\text{SO}_4^{\bullet-}$, $\bullet\text{OH}$, and along with holes played the major roles in the prior and mid-late periods of the PMS-photocatalytic oxidation process.

The degradation inhibition ratio in Fig. 8c offered a more intuitive understanding on the overall contribution of each active substance to the oxidation of 5-FLU in the 1.0CNQDs@C₁F₁O/PMS/vis system. On these grounds, it was believed that $\text{SO}_4^{\bullet-}$, $\bullet\text{OH}$, and photogenerated holes were the dominant ROS in the whole reaction, and the formed $^1\text{O}_2$ and $\text{O}_2^{\bullet-}$ were also useful for the 5-FLU degradation. To validate the proposed hypothesis, the time-dependent change in the PMS decomposition and the contributions of ROS are recorded in Fig. 8d. In the early stage of the catalytic degradation, PMS could be effectively activated to produce

$\text{SO}_4^{\bullet-}$ as the dominant active species to react with 5-FLU. As the reaction proceeded, PMS was consumed at a constant rate, and the contribution of $\text{SO}_4^{\bullet-}$ also tended to decrease, while the contributions of $\bullet\text{OH}$ and photoinduced holes increased gradually in the middle and late stages of the experiment. The $\text{SO}_4^{\bullet-}$ and $\bullet\text{OH}$ generated during the reaction were further quantified via probe experiments to better illustrate their contribution to 5-FLU degradation. It can be seen from Fig. S16 that the $\text{SO}_4^{\bullet-}$ production in the 1.0CNQDs@C₁F₁O/PMS/vis system showed a declining trend as the reaction proceeded, while the concentration of $\bullet\text{OH}$ gradually increased. These results revealed that the essence of 5-FLU degradation in the studied system was the relay process combined PMS with photocatalysis.

Furthermore, DMPO and TEMP were utilized as the spin-trapping agents to ascertain the types of ROS in the 1.0CNQDs@C₁F₁O/PMS/vis system by using EPR technique. The results in Fig. 8e displayed that the characteristic signals of both DMPO- $\bullet\text{OH}$ and DMPO- $\text{SO}_4^{\bullet-}$ appeared in the 1.0CNQDs@C₁F₁O/PMS/vis system at the beginning of the reaction. Notably, with the illumination time prolonged, the signal intensity of DMPO- $\text{SO}_4^{\bullet-}$ gradually weakened, while the intensity of characteristic DMPO- $\bullet\text{OH}$ peak was strengthened slightly, verifying that the photocatalytic oxidation gradually became the dominant process as

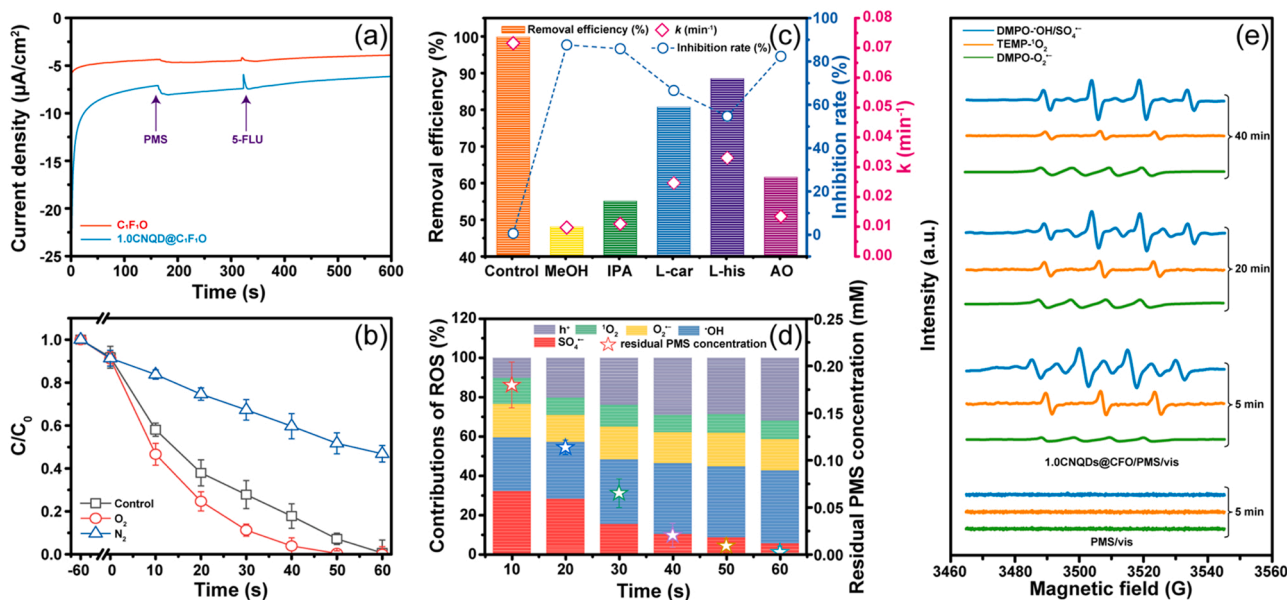


Fig. 8. (a) Chronoamperometric analysis. (b) Effect of different gas environment on 5-FLU degradation. (c) The catalytic performance of the 1.0CNQDs@C₁F₁O/PMS/vis system with different scavengers, corresponding k values and degradation inhibition ratios. (d) The contributions of various ROS and residual PMS concentration in solution. (e) The EPR signals of $\text{SO}_4^{\bullet-}$, $\bullet\text{OH}$, $^1\text{O}_2$, and $\text{O}_2^{\bullet-}$ in different time and systems. (Conditions: 30 μM 5-FLU, 0.2 g L⁻¹ catalyst, 0.3 mM PMS, pH = 6.4, and 25 °C).

the PMS consumption during the 5-FLU degradation. Meanwhile, the typical signals assigned to TEMP- $^1\text{O}_2$ and DMPO- $\text{O}_2^{\bullet-}$ were also clearly seen, meaning the generation of $^1\text{O}_2$ and $\text{O}_2^{\bullet-}$ species in the 1.0CNQDs@C₁F₁O/PMS/vis system. In contrast, these EPR feature signals were hardly detected in the PMS/vis system, suggesting that PMS could not be activated directly by visible light. On the whole, in the PMS-photocatalysis coupling system, the fabricated material demonstrated sterling PMS activation and photocatalytic ability for highly reactive substance like $\bullet\text{OH}$, $\text{SO}_4^{\bullet-}$, $\text{O}_2^{\bullet-}$, $^1\text{O}_2$, and holes production.

Since the structure evolution of 1.0CNQDs@C₁F₁O during PMS activation could induce the formation of dual Z-scheme heterostructures, the photoelectrochemical properties of the reacted 1.0CNQDs@C₁F₁O material was obviously enhanced. To further validate this result, the EPR spectra and chronoamperometric analysis of the fresh and used 1.0CNQDs@C₁F₁O were performed. As shown in Fig. S17a, the signal of DMPO- $\bullet\text{OH}$ could be easily detected for the used catalyst under visible light irradiation without the addition of PMS, while no signal could be detected in the 1.0CNQDs@C₁F₁O/vis system, suggesting that PMS induced strategy could alter the band structure of 1.0CNQDs@C₁F₁O, enabling it to generate $\bullet\text{OH}$ in a single photocatalytic process. From the Fig. S17b, it can be clearly observed that the used 1.0CNQDs@C₁F₁O exhibited stronger current responses than the fresh sample. The above phenomenon further proved the superior photocatalytic performance of the used 1.0CNQDs@C₁F₁O in comparison of the fresh material. Furthermore, the catalytic properties of the fresh and used 1.0CNQDs@C₁F₁O in the photocatalytic and PMS-photocatalytic processes was compared (Fig. S18). The degradation performance of the used material was better than that of the fresh material in the photocatalysis, but was inferior to the fresh material in the PMS-photocatalytic coupling process, which was mainly due to the important role of Cu⁰ in the PMS activation, making 1.0CNQDs@C₁F₁O more suitable for the relay oxidation process.

For a deeper study, the changes in electronic band structure of the C₁F₁O, 1.0CNQDs@C₁F₁O, and used 1.0CNQDs@C₁F₁O samples were calculated by DFT. As expected, the band gap value of 1.0CNQDs@C₁F₁O was narrower than that of the pristine C₁F₁O (Fig. S19a and S19b) owing to the quantum confinement and up-conversion effects of the loaded CNQDs, thereby increasing the

efficiencies of light harvesting and carrier transfer. The optimized crystal models of C₁F₁O and 1.0CNQDs@C₁F₁O were established in Fig. S19c and S19d. More precisely, the band gap energies of each component for the fresh and used samples were obtained from theoretical calculation. From Fig. 9a–c, the VB of CuFe₂O₄, CNQDs, and CuO were 0.30, 1.45 and 1.83 eV, respectively, and the corresponding CB were -1.22, -1.09, and 0.51 eV, respectively. These computed values were near to the experimental data and previous literatures [48,49]. According to the above information, the energy level distributions of 1.0CNQDs@C₁F₁O and used 1.0CNQDs@C₁F₁O were displayed in Fig. 9d and e. The results of DFT calculation could make mutual validation with characterizations analysis.

DFT calculations were implemented to get an in-depth understanding of the adsorption and activation behaviors of PMS on the surfaces of C₁F₁O and 1.0CNQDs@C₁F₁O photocatalysts. According to the optimized adsorption configurations of C₁F₁O/PMS and 1.0CNQDs@C₁F₁O/PMS (Fig. 10a and b), the adsorption energies (E_{ads}) of PMS over the C₁F₁O and 1.0CNQDs@C₁F₁O matrices were calculated to be -0.651 and -1.236 eV, respectively. This indicated that 1.0CNQDs@C₁F₁O had a lower energy barrier for PMS adsorption compared with C₁F₁O, which was favorable for accelerating PMS activation process. Meanwhile, from the charge density difference analysis (Fig. 10c and d), it can be seen that in the synthesized materials, Cu⁰ could act as an electron conduction bridge, and CNQDs would further promote the interfacial charge transfer, resulting in 1.0CNQDs@C₁F₁O exhibiting higher chemisorption capacity for PMS than that of C₁F₁O. Thus, the CNQDs and Cu⁰ with good conductivity in the 0D/3D CNQDs/CuFe₂O₄/Cu⁰ heterostructures could use as the major active sites to activate PMS. Subsequently, the changes in PMS bond lengths throughout the activation process was studied to evaluate the propensity of bond scission and ROS generation. As shown in Fig. 10e, the O-O bond lengths of the free PMS, adsorbed PMS, transition state, and resultant were 1.621, 1.485, 2.120, and 3.359 eV, respectively. These data suggested that the O-O bond was broken and the -OH group was detached from the PMS molecule. Specifically, PMS became unstable when it bonded with the activator, and the -OH group of PMS was strongly attracted, resulting in the cleavage of PMS to produce $\bullet\text{OH}$ and $\text{SO}_4^{\bullet-}$. It was notable that the O-O bond of the adsorbed PMS underwent a slight contraction, which

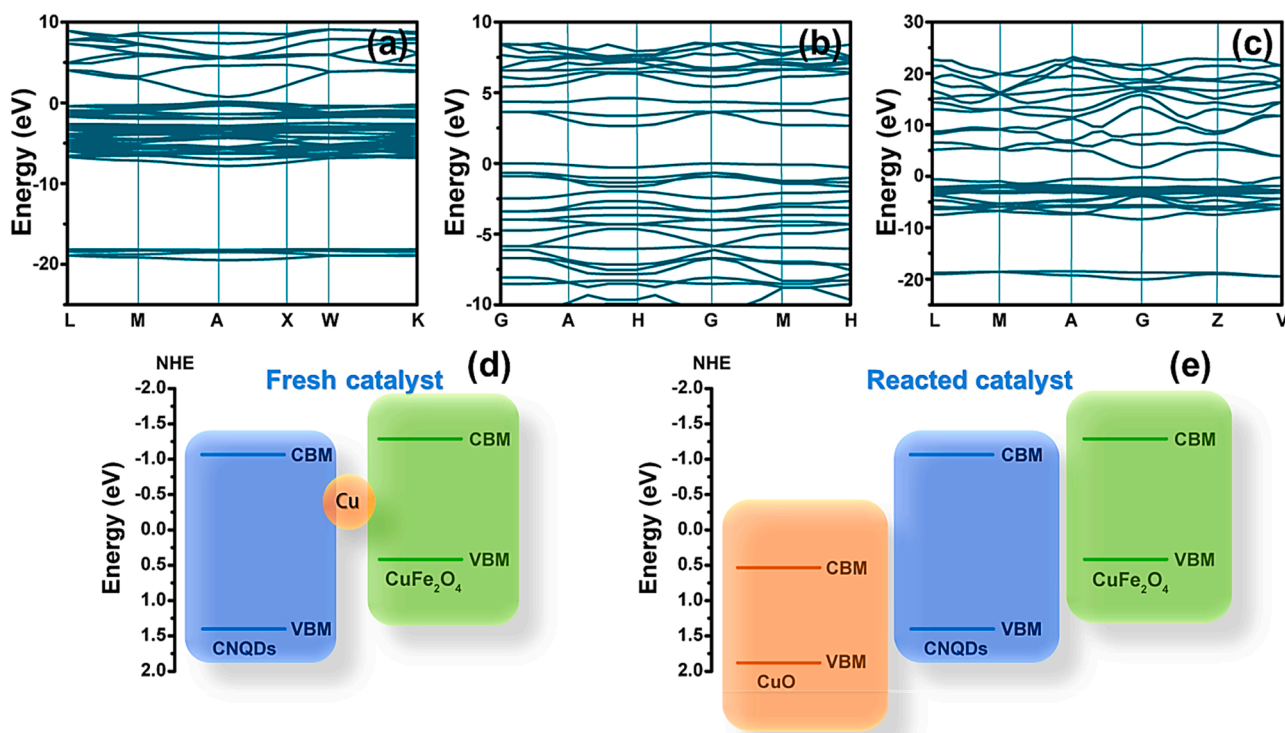
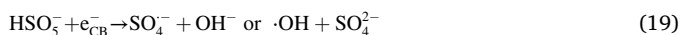


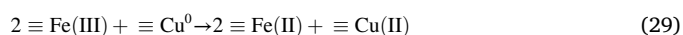
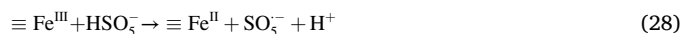
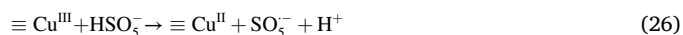
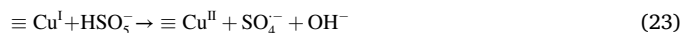
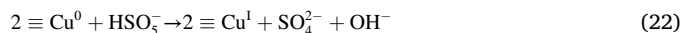
Fig. 9. The electronic band structures of (a) CuFe_2O_4 , (b) CNQDs, and (c) CuO . (d) The energy level distributions of the fresh and used $1.0\text{CNQDs}@C_1F_1O$ samples (d and e).

might be caused by the strong interaction between the Cu^0 site and the S-O bond of PMS. Moreover, the adsorption and dissociation of PMS over the $1.0\text{CNQDs}@C_1F_1O$ surface were endothermic with free energies of -1.37 and -1.47 eV, respectively, meaning that these processes could proceed spontaneously (Fig. 10f).

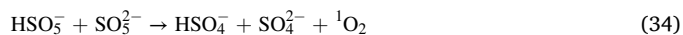
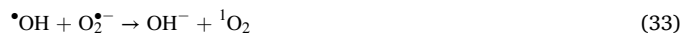
Comprehensive analysis of DFT calculations, characterization and experimental results, a hypothetical mechanism for the strengthened PMS-photocatalytic properties of $1.0\text{CNQDs}@C_1F_1O$ was proposed in Fig. 11. Initially, PMS molecules had a strong chemisorption behavior on the C_1F_1O surface modified by CNQDs. The characteristics of broad spectrum light responsivity and narrow band gap of $1.0\text{CNQDs}@C_1F_1O$ made it easy to be excited by visible light to produce photoinduced electron (e_{CB}^-)-hole (h_{VB}^+) pairs (Eq. (18)). Subsequently, both the excited e_{CB}^- and h_{VB}^+ were responsible for the $\text{SO}_4^{\cdot-}$ and $\cdot\text{OH}$ release according to Eqs. (19–21).



At the same time, $\equiv\text{Cu}^0$, $\equiv\text{Fe(II)}$, and $\equiv\text{Cu(II)}$ sites on the $1.0\text{CNQDs}@C_1F_1O$ surface were also able to catalyze the conversion of HSO_5^- to $\text{SO}_4^{\cdot-}$, and the reduction of these produced high valence metallic ions also occurred by reacting with HSO_5^- (Eqs. (22)–(28)) [57]. Unfortunately, for conventional Fe^{2+} /PMS system, Eq. (11) was sluggish and the rate-limiting step. But in the $1.0\text{CNQDs}@C_1F_1O$ composite, Cu^0 function as electron donor allowed electrons to be transferred from it to $\equiv\text{Fe}^{\text{III}}$, thereby promoting the cycling of $\text{Fe(II)}/\text{Fe(III)}$ through Eq. (29) [58]. Furthermore, because the standard reduction potential of $\text{Fe(III)}/\text{Fe(II)}$ (0.77 V vs. NHE) was higher than that of $\text{Cu(II)}/\text{Cu(I)}$ (0.17 V vs. NHE), the reduction of the generated Fe(III) by Cu(I) was thermodynamically permitted (Eq. (30)) [34].



As for the $^1\text{O}_2$ produced in the coupling system, it can be converted from the formed $\text{O}_2^{\cdot-}$ and $\cdot\text{OH}$ as well as the PMS self-decomposition depend on Eqs. (31)–(34).



Significantly, as the reaction progressed, the structural evolution of photocatalyst took place due to the oxidation of Cu^0 into CuO , resulting in the formation of new interfacial nanojunction. Because of the matchable band alignment between CNQDs, CuFe_2O_4 , and CuO , an inner electrical field could be established in the composite, which derived the rapid migration of photogenerated carriers. Thereafter, two

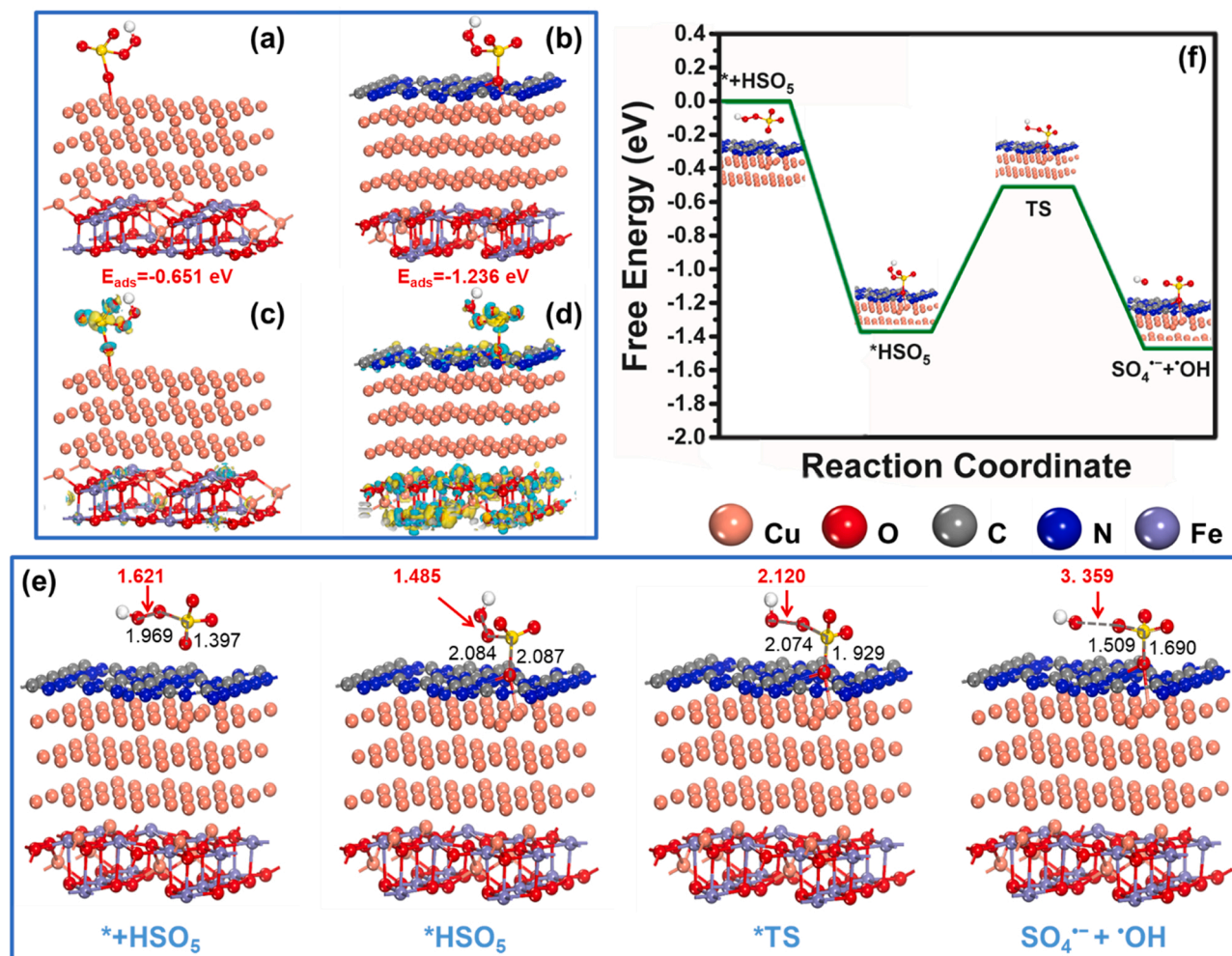


Fig. 10. The calculated adsorption energies of PMS on the (a) C_1F_1O and (b) $1.0CNQDs@C_1F_1O$, and (c and d) the corresponding charge density difference analysis (blue and yellow mean electron depletion and electron accumulation). (e) DFT calculation of PMS adsorption-dissociation process on the $1.0CNQDs@C_1F_1O$. (f) Calculated free energy for PMS activation over the $1.0CNQDs@C_1F_1O$.

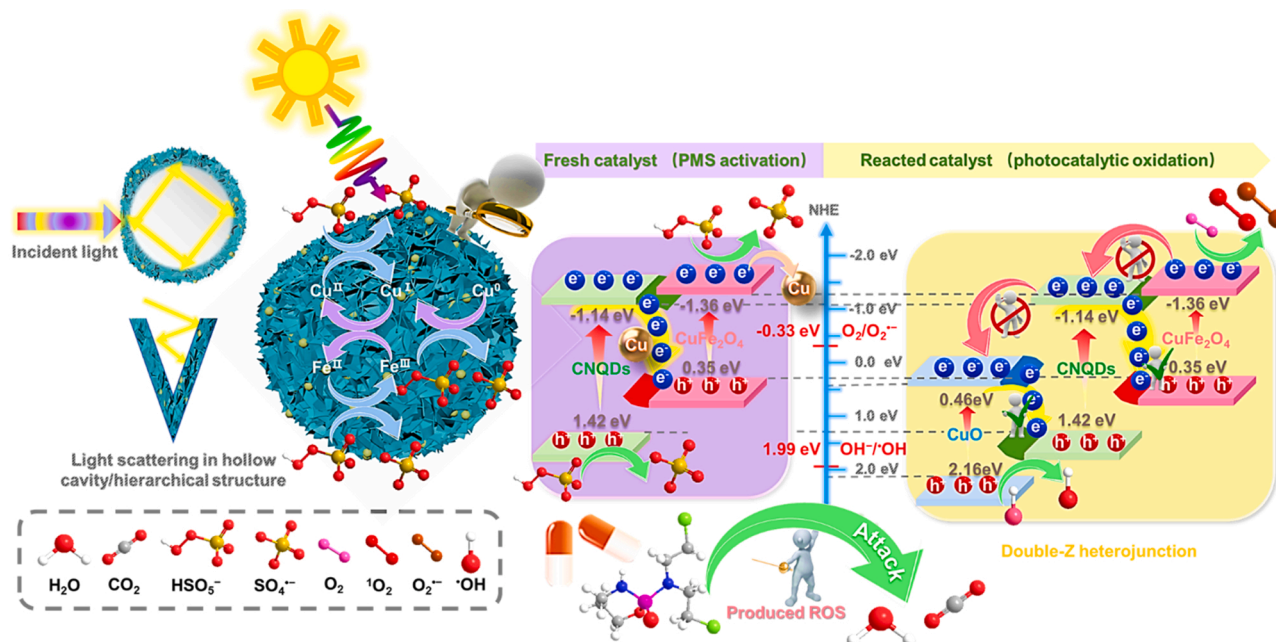
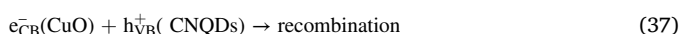
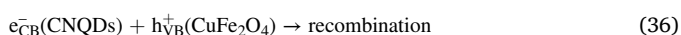
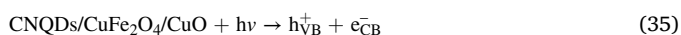


Fig. 11. Schematic of the synergistic catalytic mechanism for the $1.0CNQDs@C_1F_1O/PMS/vis$ system.

possible carrier transfer pathways were proposed according to the positions of their CB and VB. In terms of the traditional heterojunction mechanism, photoexcited e_{CB}^- and h_{VB}^+ would be gathered on the CB of CuO and the VB of CuFe₂O₄, respectively, which led to their inability to react with OH⁻/H₂O and O₂ to form reactive species. This was in conflict with the EPR measurement results (Fig. S17a and Fig. S20), which suggested that the used materials can generate \cdot OH and O₂^{•-} in the absence of PMS under visible light irradiation. Instead, the e_{CB}^- generated in the CB of CNQDs and CuO would transfer and recombine with h_{VB}^+ in the VB of CuFe₂O₄ and CNQDs, and this dual Z-scheme transfer pathway would give rise to the accumulation of e_{CB}^- on the CB of CuFe₂O₄ and the retention of h_{VB}^+ on the VB of CuO (Eq. (35)–(37)). On the one hand, the CB potential of CuFe₂O₄ ($E_{CB} = -1.36$ eV vs. NHE) was more negative than $E_0(O_2/O_2^{\cdot-})$ (-0.33 eV vs. NHE), suggesting the dissolved O₂ could be transformed into O₂^{•-} via reacting with e_{CB}^- (Eq. (38)). On the other hand, the VB potential of CuO ($E_{VB} = 2.16$ eV vs. NHE) was positive enough to yield \cdot OH through the oxidation between h_{VB}^+ and OH⁻ ($E_0(OH^-/\cdot OH) = 1.99$ eV vs. NHE) (Eq. (39)). Therefore, we have reasons to believe that the boosted photocatalytic properties of CNQDs/CuFe₂O₄/CuO could be ascribed to the unique dual Z-scheme mechanism, which not only facilitated the separation of photoinduced carriers, but also reserved their strong redox potential. During the whole reaction process, benefiting from the reasonable combination of PMS and photocatalysis, ROS would be continuously emerged, guaranteeing the efficient decomposition of stubborn organic pollutant.



4. Conclusions

To sum up, a new hybrid 0D/3D nanojunction architecture was successfully constructed by combining CNQDs with CuFe₂O₄/Cu⁰ hollow microspheres (CNQDs@CFO), and as a robust catalyst tailored for the relay process of PMS and photocatalysis. Impressively, the obtained 1.0CNQDs@C₁F₁O coupling with PMS exhibited significantly enhanced photocatalytic properties and excellent cycling stability, where the initial and fifth degradation efficiencies of 5-FLU in 60 min of visible light irradiation could reach 99.4 % and 92.6 %, respectively. Moreover, 1.0CNQDs@C₁F₁O could well resist the disturbance from the coexisting substances in aquatic environment, and showed sound reliability in a wide temperature and pH range and different real water matrix. Quenching experiments and EPR tests revealed that SO₄^{•-}, \cdot OH, and h_{VB}^+ played the leading roles in the stages of PMS oxidation and photocatalysis, respectively. Through analysis of the detection data from UPLC-MS/MS, the primary decomposition routes of 5-FLU were elucidated. Furthermore, by comparing the physicochemical properties of the fresh and used samples, it was reasonable to believe that new structure photocatalyst was generated by valence variation. Combining with various advanced characterization techniques, experimental results, and DFT calculations, a plausible improving mechanism for the 1.0CNQDs@C₁F₁O/PMS/vis system was illustrated from six aspects, hierarchical hollow architectures, broad spectrum photoresponse, efficient interfacial electron transfer, accelerated metal ions redox cycling, multiple PMS active sites, and dual Z-scheme heterostructures formed via PMS induced strategy. These striking features of 1.0CNQDs@C₁F₁O made it perfectly competent for the proposed segmented coupling oxidation system. This work offers an upgrading strategy for integrating PMS catalysis with photocatalysis by designing a novel 0D/3D heterojunction photocatalyst with changeable structure.

CRediT authorship contribution statement

Anqi Wang: Data curation, Formal analysis, Investigation, Methodology, Writing – original draft, Project administration, Funding acquisition. **Shuya Guo:** Resources, Investigation, Data curation, Writing – original draft. **Manman Xu:** Methodology, Software. **Cuilin Meng:** Data curation. **Haida Zhu:** Software, Validation, Visualization. **Tong Zheng:** Writing – review & editing. **Hui Wang:** Formal analysis. **Kai Wang:** Validation. **Wei Shi:** Validation. **Xingxin Liu:** Software. **Xiaolong Song:** Methodology, Visualization. **Zhaofeng Chang:** Conceptualization, Writing – review & editing, Supervision, Project administration, Funding acquisition.

Declaration of Competing Interest

The authors declare that they have no known competing financial interests or personal relationships that could have appeared to influence the work reported in this paper.

Data Availability

Data will be made available on request.

Acknowledgments

The authors acknowledged the financial supports from National Natural Science Foundation of China (52100173, 42107266, and 21908024) and Doctoral Research Start-up Funds (211135110) from Dongguan University of Technology.

Appendix A. Supporting information

Supplementary data associated with this article can be found in the online version at doi:10.1016/j.apcatb.2022.122117.

References

- [1] D. Liu, C. Poon, K. Lu, C. He, W. Lin, Self-assembled nanoscale coordination polymers with trigger release properties for effective anticancer therapy, *Nat. Commun.* 5 (2014) 4182.
- [2] S. Nussbaumer, P. Bonnabry, J.L. Veuthey, S. Fleury-Souverein, Analysis of anticancer drugs: a review, *Talanta* 85 (2011) 2265–2289.
- [3] J. Zhang, V.W.C. Chang, A. Giannis, J.Y. Wang, Removal of cytostatic drugs from aquatic environment: a review, *Sci. Total. Environ.* 445 (2013) 281–298.
- [4] A.Y.C. Lin, X.H. Wang, W.N. Lee, Phototransformation determines the fate of 5-fluorouracil and cyclophosphamide in natural surface waters, *Environ. Sci. Technol.* 47 (2013) 4104–4112.
- [5] M. Mišić, M. Filipić, A. Nersisyan, M. Kundi, M. Isidori, S. Knasmueller, Environmental risk assessment of widely used anticancer drugs (5-fluorouracil, cisplatin, etoposide, imatinib mesylate), *Water Res.* 164 (2019), 114953.
- [6] P. Mazierski, A.F. Borzyszkowska, P. Wilczewska, A. Białk-Bielińska, A. Zaleska-Medynska, E.M. Siedlecka, A. Pieczyńska, Removal of 5-fluorouracil by solar-driven photoelectrocatalytic oxidation using Ti/TiO₂(NT) photoelectrodes, *Water Res.* 157 (2019) 610–620.
- [7] C.A. Lutterbeck, M.L. Wilde, E. Baginska, C. Leder, E.L. Machado, K. Kuemmerer, Degradation of 5-FU by means of advanced (photo)oxidation processes: UV/H₂O₂, UV/Fe²⁺/H₂O₂ and UV/TiO₂ – comparison of transformation products, ready biodegradability and toxicity, *Sci. Total. Environ.* 578 (2017) 257–267.
- [8] G.K. Dinesh, M. Pramod, S. Chakma, Sonochemical synthesis of amphoteric Cu⁰-nanoparticles using *Hibiscus rosa-sinensis* extract and their applications for degradation of 5-fluorouracil and lovastatin drugs, *J. Hazard. Mater.* 399 (2020), 123035.
- [9] A.S. Ochoa-Chavez, A. Pieczyńska, A.F. Borzyszkowska, P.J. Espinoza-Montero, E. M. Siedlecka, Electrochemical degradation of 5-FU using a flow reactor with BDD electrode: Comparison of two electrochemical systems, *Chemosphere* 201 (2018) 816–825.
- [10] A. Koltakidou, M. Antonopoulou, E. Epsilonigenidou, I. Konstantinou, A. E. Giannakas, M. Papadaki, D. Bikiaris, D.A. Lambropoulou, Photocatalytic removal of fluorouracil using TiO₂-P25 and N/S doped TiO₂ catalysts: a kinetic and mechanistic study, *Sci. Total. Environ.* 578 (2017) 257–267.
- [11] S. Chen, L. Blaney, P. Chen, S. Deng, M. Hopanna, Y. Bao, G. Yu, Ozonation of the 5-fluorouracil anticancer drug and its prodrug capecitabine: reaction kinetics, oxidation mechanisms, and residual toxicity, *Front. Environ. Sci. Eng.* 13 (2019) 59.

- [12] G.K. Dinesh, S. Chakma, Mechanistic investigation in degradation mechanism of 5-Fluorouracil using graphitic carbon nitride, *Ultrason. Sonochem.* 50 (2019) 311–321.
- [13] E.S. Emidio, P. Hammer, R.F.P. Nogueira, Simultaneous degradation of the anticancer drugs 5-fluorouracil and cyclophosphamide using a heterogeneous photo-Fenton process based on copper-containing magnetites ($\text{Fe}_{3-x}\text{Cu}_x\text{O}_4$), *Chemosphere* 241 (2020), 124990.
- [14] J.P. Besse, J.F. Latour, J. Garric, Anticancer drugs in surface waters: What can we say about the occurrence and environmental significance of cytotoxic, cytostatic and endocrine therapy drugs? *Environ. Int.* 39 (2012) 73–86.
- [15] J. Zhang, V.W.C. Chang, A. Giannis, J.Y. Wang, Removal of cytostatic drugs from aquatic environment: a review, *Sci. Total. Environ.* 445–446 (2013) 281–298.
- [16] A. Wang, Z. Zheng, H. Wang, Y. Chen, C. Luo, D. Liang, B. Hu, R. Qiu, K. Yan, 3D hierarchical H_2 -reduced Mn-doped CeO_2 microflowers assembled from nanotubes as a high-performance Fenton-like photocatalyst for tetracycline antibiotics degradation, *Appl. Catal. B: Environ.* 277 (2020), 119171.
- [17] J. Zhang, C. Zhai, W. Zhao, Y. Chen, R. Yin, L. Zeng, M. Zhu, Insight into combining visible-light photocatalysis with transformation of dual metal ions for enhancing peroxymonosulfate activation over dibismuth copper oxide, *Chem. Eng. J.* 397 (2020), 125310.
- [18] M. Ding, W. Ao, H. Xu, W. Chen, L. Tao, Z. Shen, H. Liu, C. Lu, Z. Xie, Facile construction of dual heterojunction $\text{CoO}/\text{TiO}_2/\text{MXene}$ hybrid with efficient and stable catalytic activity for phenol degradation with peroxymonosulfate under visible light irradiation, *J. Hazard. Mater.* 420 (2021), 126686.
- [19] A. Wang, H. Wang, H. Deng, S. Wang, W. Shi, Z. Yi, R. Qiu, K. Yan, Controllable synthesis of mesoporous manganese oxide microsphere efficient for photo-Fenton-like removal of fluoroquinolone antibiotics, *Appl. Catal. B: Environ.* 248 (2019) 298–308.
- [20] A. Wang, S. Guo, Z. Zheng, H. Wang, X. Song, H. Zhu, Y. Zeng, J. Lam, R. Qiu, K. Yan, Highly dispersed Ag and $\text{g-C}_3\text{N}_4$ quantum dots co-decorated 3D hierarchical Fe_3O_4 hollow microspheres for solar-light-driven pharmaceutical pollutants degradation in natural water matrix, *J. Hazard. Mater.* 434 (2022), 128905.
- [21] G. Chen, Y. Yu, L. Liang, X. Duan, R. Li, X. Lu, B. Yan, N. Li, S. Wang, Remediation of antibiotic wastewater by coupled photocatalytic and persulfate oxidation system: A critical review, *J. Hazard. Mater.* 408 (2021), 124461.
- [22] J. Zhao, Z. Zhao, N. Li, J. Nan, R. Yu, J. Du, Visible-light-driven photocatalytic degradation of ciprofloxacin by a ternary $\text{Mn}_2\text{O}_3/\text{Mn}_3\text{O}_4/\text{MnO}_2$ valence state heterojunction, *Chem. Eng. J.* 353 (2018) 805–813.
- [23] L. Li, C.G. Niu, H. Guo, J. Wang, M. Ruan, L. Zhang, C. Liang, H.Y. Liu, Y.Y. Yang, Efficient degradation of Levofloxacin with magnetically separable $\text{ZnFe}_2\text{O}_4/\text{NCDs}/\text{Ag}_2\text{CO}_3$ Z-scheme heterojunction photocatalyst: Vis-NIR light response ability and mechanism insight, *Chem. Eng. J.* 383 (2020), 123192.
- [24] Y.Y. Yang, X.G. Zhang, C.G. Niu, H.P. Feng, P.Z. Qin, H. Guo, C. Liang, L. Zhang, H. Y. Liu, L. Li, Dual-channel charges transfer strategy with synergistic effect of Z-scheme heterojunction and LSPR effect for enhanced quasi-full-spectrum photocatalytic bacterial inactivation: new insight into interfacial charge transfer and molecular oxygen activation, *Appl. Catal. B: Environ.* 264 (2020), 118465.
- [25] C. Liu, H. Dai, C. Tan, Q. Pan, F. Hu, X. Peng, Photo-Fenton degradation of tetracycline over Z-scheme $\text{Fe-g-C}_3\text{N}_4/\text{Bi}_2\text{WO}_6$ heterojunctions: mechanism insight, degradation pathways and DFT calculation, *Appl. Catal. B: Environ.* 310 (2022), 121326.
- [26] A. Wang, H. Li, J. Xiao, Y. Lu, M. Zhang, K. Hu, K. Yan, Integration of theory and experiment on mesoporous nickel sulfide microsphere for hydrogen evolution reaction, *ACS Sustain. Chem. Eng.* 6 (2018) 15995–16000.
- [27] S. Dong, J. Sun, Y. Li, C. Yu, Y. Li, J. Sun, ZnSnO_3 hollow nanospheres/reduced graphene oxide nanocomposites as high-performance photocatalysts for degradation of metronidazole, *Appl. Catal. B: Environ.* 144 (2014) 386–393.
- [28] H. Wang, B. Liao, T. Lu, Y. Ai, G. Liu, Enhanced visible-light photocatalytic degradation of tetracycline by a novel hollow $\text{BiOCl}/\text{CeO}_2$ heterostructured microspheres: Structural characterization and reaction mechanism, *J. Hazard. Mater.* 385 (2020), 121552.
- [29] T. Xiao, Z. Tang, Y. Yang, L. Tang, Y. Zhou, Z. Zou, In situ construction of hierarchical $\text{WO}_3/\text{g-C}_3\text{N}_4$ composite hollow microspheres as a Z-scheme photocatalyst for the degradation of antibiotics, *Appl. Catal. B: Environ.* 220 (2018) 417–428.
- [30] S. Zhang, Q. Wang, F. Dai, Y. Gu, G. Qian, C. Chen, Y. Yu, Novel TiO_2 nanoparticles/polysulfone composite hollow microspheres for photocatalytic degradation, *Polymers* 13 (2021) 336.
- [31] X. Wang, A. Wang, J. Ma, Visible-light-driven photocatalytic removal of antibiotics by newly designed $\text{C}_3\text{N}_4/\text{MnFe}_2\text{O}_4$ -graphene nanocomposites, *J. Hazard. Mater.* 336 (2017) 81–92.
- [32] Z.T. Dong, C.G. Niu, H. Guo, H.Y. Niu, S. Liang, C. Liang, H.Y. Liu, Y.Y. Yang, Anchoring CuFe_2O_4 nanoparticles into N-doped carbon nanosheets for peroxymonosulfate activation: Built-in electric field dominated radical and non-radical process, *Chem. Eng. J.* 426 (2021), 130850.
- [33] Y. Huang, X. Li, C. Zhang, M. Dai, Z. Zhang, Y. Xi, B. Quan, S. Lu, Y. Liu, Degrading arsenic acid and adsorbing the released inorganic arsenic simultaneously in aqueous media with CuFe_2O_4 activating peroxymonosulfate system: Factors, performance, and mechanism, *Chem. Eng. J.* 424 (2021), 128537.
- [34] X. Liu, J. Zhou, D. Liu, L. Li, W. Liu, S. Liu, C. Feng, Construction of Z-scheme $\text{CuFe}_2\text{O}_4/\text{MnO}_2$ photocatalyst and activating peroxymonosulfate for phenol degradation: synergistic effect, degradation pathways, and mechanism, *Environ. Res.* 200 (2021), 111736.
- [35] Y. Yao, F. Lu, Y. Zhu, F. Wei, X. Liu, C. Lian, S. Wang, Magnetic core-shell $\text{CuFe}_2\text{O}_4/\text{C}_3\text{N}_4$ hybrids for visible light photocatalysis of Orange II, *J. Hazard. Mater.* 297 (2015) 224–233.
- [36] T. Wang, C. Nie, Z. Ao, S. Wang, T. An, Recent progress in $\text{g-C}_3\text{N}_4$ quantum dots: synthesis, properties and applications in photocatalytic degradation of organic pollutants, *J. Mater. Chem. A* 8 (2020) 485–502.
- [37] Y. Li, K. Lv, W. Ho, F. Dong, X. Wu, Y. Xia, Hybridization of rutile TiO_2 (rTiO_2) with $\text{g-C}_3\text{N}_4$ quantum dots (CN QDs): an efficient visible-light-driven Z-scheme hybridized photocatalyst, *Appl. Catal. B: Environ.* 202 (2017) 611–619.
- [38] X. Zhang, H. Wang, H. Wang, Q. Zhang, J. Xie, Y. Tian, J. Wang, Y. Xie, Single-layered graphitic- C_3N_4 quantum dots for two-photon fluorescence imaging of cellular nucleus, *Adv. Mater.* 26 (2014) 4438–4443.
- [39] G. Li Puma, A. Brucato, Dimensionless analysis of slurry photocatalytic reactors using two-flux and six-flux radiation absorption-scattering models, *Catal. Today* 122 (2007) 78–90.
- [40] J. Colina-Márquez, F. Machuca-Martínez, G. Li Puma, Radiation absorption and optimization of solar photocatalytic reactors for environmental applications, *Environ. Sci. Technol.* 44 (2010) 5112–5120.
- [41] G. Li Puma, V. Puddu, H.K. Tsang, A. Gora, B. Toepfer, Photocatalytic oxidation of multicomponent mixtures of estrogens (estrone (E1), 17 β -estradiol (E2), 17 α -ethynylestradiol (EE2) and estril (E3)) under UVA and UVC radiation: photon absorption, quantum yields and rate constants independent of photon absorption, *Appl. Catal. B: Environ.* 99 (2010) 388–397.
- [42] M. Misra, S.R. Chowdhury, T.I. Lee, Sunlight driven decomposition of toxic organic compound, coumarin, p-nitrophenol, and photo reduction of Cr (VI) ions, using a bridge structure of Au@CNT@TiO_2 nanocomposite, *Appl. Catal. B: Environ.* 272 (2020), 118991.
- [43] R. Acosta-Herazo, M.Á. Mueses, G. Li Puma, F.M. Martínez, Impact of photocatalyst optical properties on the efficiency of solar photocatalytic reactors rationalized by the concepts of initial rate of photon absorption (IRPA) dimensionless boundary layer of photon absorption and apparent optical thickness, *Chem. Eng. J.* 356 (2019) 839–849.
- [44] L. Wang, X. Ma, G. Huang, R. Lian, J. Huang, H. She, Q. Wang, Construction of ternary $\text{CuO}/\text{CuFe}_2\text{O}_4/\text{g-C}_3\text{N}_4$ composite and its enhanced photocatalytic degradation of tetracycline hydrochloride with persulfate under simulated sunlight, *J. Environ. Sci.* 112 (2022) 59–70.
- [45] X. Zhang, B. Ren, X. Li, B. Liu, S. Wang, P. Yu, Y. Xu, G. Jiang, High-efficiency removal of tetracycline by carbon-bridge-doped $\text{g-C}_3\text{N}_4/\text{Fe}_3\text{O}_4$ magnetic heterogeneous catalyst through photo-Fenton process, *J. Hazard. Mater.* 418 (2021), 126333.
- [46] R. Li, M. Cai, Z. Xie, Q. Zhang, Y. Zeng, H. Liu, G. Liu, W. Lv, Construction of heterostructured $\text{CuFe}_2\text{O}_4/\text{g-C}_3\text{N}_4$ nanocomposite as an efficient visible light photocatalyst with peroxydisulfate for the organic oxidation, *Appl. Catal. B: Environ.* 244 (2019) 974–982.
- [47] Y. Wang, P. Du, H. Pan, L. Fu, Y. Zhang, J. Chen, Y. Du, N. Tang, G. Liu, Increasing solar absorption of atomically thin 2D carbon nitride sheets for enhanced visible-light photocatalysis, *Adv. Mater.* 31 (2019), 1807540.
- [48] A. Serrà, E. Gómez, J. Michler, L. Philippe, Facile cost-effective fabrication of $\text{Cu@Cu}_2\text{O}/\text{CuO}$ -microalgae photocatalyst with enhanced visible light degradation of tetracycline, *Chem. Eng. J.* 413 (2021), 127477.
- [49] R. Guo, Y. Chen, L.-C. Nengzi, L. Meng, Q. Song, J. Gou, X. Cheng, In situ preparation of carbon-based Cu-Fe oxide nanoparticles from CuFe Prussian blue analogues for the photo-assisted heterogeneous peroxymonosulfate activation process to remove lomefloxacin, *Chem. Eng. J.* 398 (2020), 125556.
- [50] J. Lu, Y. Zhou, Y. Zhou, Efficiently activate peroxymonosulfate by $\text{Fe}_3\text{O}_4/\text{MoS}_2$ for rapid degradation of sulfonamides, *Chem. Eng. J.* 422 (2021), 130126.
- [51] M. Gu, U. Farooq, S. Lu, X. Zhang, Z. Qiu, Q. Sui, Degradation of trichloroethylene in aqueous solution by rGO supported nZVI catalyst under several oxic environments, *J. Hazard. Mater.* 349 (2018) 35–44.
- [52] C.A. Lutterbeck, M.L. Wilde, E. Baginski, C. Leder, E.L. Machado, K. Kummerer, Degradation of cyclophosphamide and 5-fluorouracil by UV and simulated sunlight treatments: assessment of the enhancement of the biodegradability and toxicity, *Environ. Pollut.* 208 (2016) 467–476.
- [53] H.H. Lin, A.Y. Lin, Photocatalytic oxidation of 5-fluorouracil and cyclophosphamide via UV/ TiO_2 in an aqueous environment, *Water Res.* 48 (2014) 559–568.
- [54] O. Ganzhenko, N. Oturan, I. Sirés, D. Huguenot, E.D. van Hullebusch, G. Esposito, M. A. Oturan, Fast and complete removal of the 5-fluorouracil drug from water by electro-Fenton oxidation, *Environ. Chem. Lett.* 16 (2017) 281–286.
- [55] E. Evgenidou, A. Ofrydopoulou, N. Malesic-Eleftheriadou, C. Nannou, N.M. Ainali, E. Christodoulou, D.N. Bikiaris, G.Z. Kyzas, D.A. Lambropoulou, New insights into transformation pathways of a mixture of cytostatic drugs using Polyester- TiO_2 films: identification of intermediates and toxicity assessment, *Sci. Total. Environ.* 741 (2020), 140394.
- [56] W. Wang, Y. Liu, Y. Yue, H. Wang, G. Cheng, C. Gao, C. Chen, Y. Ai, Z. Chen, X. Wang, The confined interlayer growth of ultrathin two-dimensional Fe_3O_4 nanosheets with enriched oxygen vacancies for peroxymonosulfate activation, *ACS Catal.* 11 (2021) 11256–11265.
- [57] Z. Li, C. Guo, J. Lyu, Z. Hu, M. Ge, Tetracycline degradation by persulfate activated with magnetic $\text{Cu}/\text{CuFe}_2\text{O}_4$ composite: efficiency, stability, mechanism and degradation pathway, *J. Hazard. Mater.* 373 (2019) 85–96.
- [58] L. Cui, Z. Li, Q. Li, M. Chen, W. Jing, X. Gu, $\text{Cu}/\text{CuFe}_2\text{O}_4$ integrated graphite felt as a stable bifunctional cathode for high-performance heterogeneous electro-Fenton oxidation, *Chem. Eng. J.* 420 (2021), 127666.